ABSTRACT

COMBUSTION OF FINE MAGNESIUM PARTICLES

by

Song Wang

Recent interest in developing Al-Mg alloys as reactive materials prompted studies of combustion mechanisms for particles of such alloys with different Al/Mg ratios. Reference experiments with pure Al and Mg powders are also desired to better understand and model combustion of the respective alloys. While combustion of pure Al powders has been addressed in many recent studies, combustion of magnesium explored mostly coarse, 50 μm, and larger particles. This effort is focused to characterize and understand combustion dynamics for fine Mg powders. Spherical, micron-sized magnesium particles were introduced in an air-acetylene flame using a custom-made screw feeder. Particles were observed to burn in laminar flames as well as in the flames with turbulence induced by a swirling air flow. Particle emission was well detectable above the flame emission background and emission pulses for individual particles were recorded using an array of three filtered photomultiplier tubes. Particle size distribution was correlated with particle emission times (and thus, burn times) for different turbulence levels. The effect of turbulence on the measured burn times was stronger for the finer particles. Partially burned particles were collected and examined using an electron microscope. The particle spherical shapes were not preserved, with greater discrepancies from spherical shapes observed for finer particles. It was also observed that the presence of greater amounts of MgO on surface of metal particles results in a noticeable increase

in the particle burn time. This effect is difficult to interpret considering that the initial MgO amount is negligible compared to the MgO formed on the particle surface during its combustion. It is proposed that the initial MgO present in the shape of small particles adhered to the metal surface results in the formation of MgO islands and inclusions on surface of the burning Mg droplets. Such islands block evaporation of magnesium and thus reduce the burn rates. In addition, they serve as condensation centers for the combustion products and thus tend to grow rapidly during combustion. As a result, a relatively small number of the initial fine MgO particles can cause substantial disruption in the burning particle shape, surface morphology, and burn rate. The measured color temperatures inferred from the burning particle emission exceed significantly the boiling point of Mg, but are much lower than the adiabatic flame temperatures. It is also observed that the temperatures decrease for the particles burning in turbulent flows. It is suggested that the measured temperatures represent those of the MgO inclusions embedded in the boiling Mg; their reduction in the higher turbulence flow is associated with an accelerated rate of heat transfer.

COMBUSTION OF FINE MAGNESIUM PARTICLES

by
Song Wang

A Master Thesis
Submitted to the Faculty of
New Jersey Institute of Technology
in Partial Fulfillment of the Requirements for the Degree of
Master of Science in Chemical Engineering

Department of Chemical, Biological and Pharmaceutical Engineering

May 2014

APPROVAL PAGE

COMBUSTION OF FINE MAGNESIUM PARTICLES

Song Wang

Dr. Edward L Dreizin, Master Thesis Advisor Date
Professor of Chemical, Biological and Pharmaceutical Engineering, NJIT

Dr. Laurent Simon, Committee Member Date
Associate Professor of Chemical, Biological and Pharmaceutical Engineering, NJIT

Dr. Mirko Schoenitz, Committee Member Date
Research Professor of Chemical, Biological and Pharmaceutical Engineering, NJIT

BIOGRAPHICAL SKETCH

Author: Song Wang

Degree: Master of Science

Date: April 17, 2014

Undergraduate and Graduate Education:

- Master of Science in Chemical, Biological and Pharmaceutical Engineering, New Jersey Institute of Technology, Newark, NJ, 2014
- Bachelor of Science in Chemical Engineering, Qingdao University, Qingdao, P. R. China, 2012

Major: Chemical Engineering

TABLE OF CONTENTS

TABLE OF CONTENTS
(Continued)

Chapter **Page**

LIST OF FIGURES

LIST OF FIGURES
(Continued)

LIST OF FIGURES
(Continued)

Figure **Page**

CHAPTER 1

INTRODUCTION

The interest in improved metal fuels is stimulated by development of advanced solid propellants [1-4], explosives [5-8]and pyrotechnics [9-11]. While aluminum is by far the most widely used metal additives in energetic formulation, in many papers it was shown that advanced combustion performance can be achieved when aluminum-magnesium alloys are used [12-18]. In particular, mechanically alloyed Al-Mg powders were recently shown to exhibit attractive burn rates [19, 20].

Compared to the pure Al powders, such alloys may burn faster, exhibit less significant agglomeration, and burn at higher temperatures. To design the energetic material and respective system using Al-Mg alloys as fuel additives, a mechanistic model describing their combustion rate as a function of the oxidizer composition, flow turbulence, and pressure is necessary. Such models are being currently developed for pure Al particle combustion [21], for which different combustion regimes were reported [22, 23]; however, very little in the way of model development is done for Al-Mg alloys.

In order to develop a useful combustion model for the alloys, burning behavior of both pure metal components must be understood. Research on combustion of Mg has been active for a long time; however, there are relatively few experimental studies quantifying combustion rates and temperatures for Mg particles [24-28]. Most of the previous experiments employed rather coarse Mg particles, with dimensions close to 1 mm. It was reported that such particles burn according to the well-known d^2 law; in other words their burn time, τ, is proportional to the

square of the initial particle diameter, *d*. The flame sizes observed for burning Mg particles exceed significantly the particle size

[29-31] and the temperatures reported to be 2630 – 2800 K [32, 33] or even 3400 K [26], close to the predicted adiabatic flame temperatures of 3100 – 3610 K [33, 34].

Based on the published results, it is common to assume that Mg particles burn in the vapor phase, similar to the liquid fuel droplets. However, it was reported that the combustion products collected from burning Mg powders are not spherical [26, 29], which cannot be readily explained considering the droplet combustion model. Experimental data with fine Mg particles are also lacking. Recent experiments on combustion of fine Mg powder in water showed a substantially reduced effect of particle size on the burn time [35], consistently with recent experiments on fine Al particles [36-38].

The objective of this project is to characterize experimentally combustion of fine Mg particles in an oxidizer comprising mixed carbon dioxide and water, which is the environment similar to that encountered by the burning metal particles in propellants and explosives. Combustion will be studied in both laminar flame and in the flame with turbulent mixing of the reaction products with surrounding air.

CHPATER 2

EXPERIMENTAL

2.1 Approach

Metal particles are ignited in an air-acetylene flame and their combustion is examined based on their optical emission. The turbulence in the combustion environment is varied. The experimental setup is schematically shown in Figure 2.1. It was described earlier [35, 39] and only minor modifications were made for this project.

Spherical magnesium powder is fed through a central axis of an air-acetylene flame where particles ignite and burn in the combustion products comprising mostly carbon dioxide and water, while surrounding air is mixed in the combustion environment providing additional oxidizer. Initial flows of both premixed air-acetylene and nitrogen carrying particles are directed vertically. Turbulence is introduced by air fed through three auxiliary nozzles placed horizontally around the flame and directed tangentially within a short cylindrical enclosure. The flow rate of the auxiliary air jets is adjusted to alter the level of the achieved turbulence. The generated flow pattern inducing the flame turbulence is cylindrically symmetric. This method of producing turbulence is similar to that used in References [40, 41], where, tangentially directed fans were installed inside an explosion vessel. In addition to the new flow pattern, this approach enhances mixing of the flame and burning particles with the surrounding air. The effects of a turbulent flow pattern and of an enhanced mixing with surrounding air cannot be separated from each other in the present experiment.

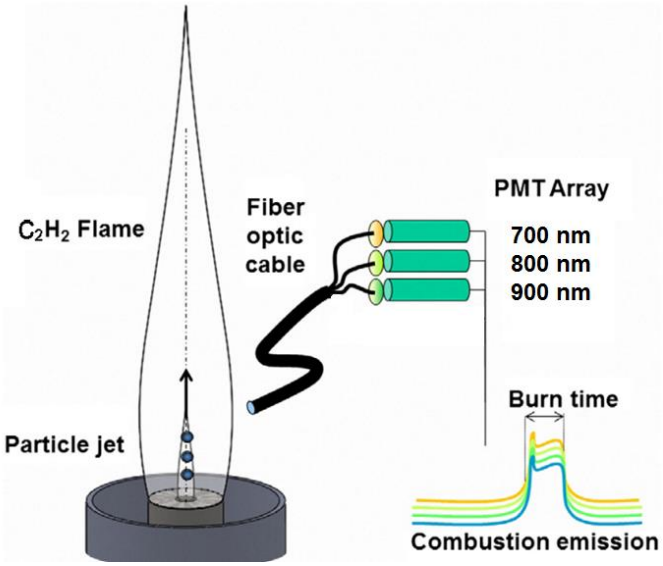

Figure 2.1 Schematic of the experimental apparatus.

Sources: Amy Corcoran, Stefano Mercati, Hongqi Nie, Massimo Milani, Luca Montorsi, and Edward L Dreizin "Combustion of fine aluminum and magnesium powders in water" New Jersey Institute of Technology. Combustion and Flame 160(2013)2242-2250.
www.elsevier.com/locate/combustflame.

Particle emission signatures were recorded using an array of three filtered photomultiplier tubes (PMT's). Assuming, that larger particles burn longer, the measured statistical distribution of particle burn times was correlated with the distribution of particle sizes. This correlation produced a trend for the particle burn times as a function of their diameters. Further, emission intensity ratios measured at different wavelengths were used to evaluate the burning particle temperatures.

Note that most particles ignite while being introduced into the laminar flame zone and continue burning passing through the turbulent regions. The measured burn times do not discriminate between these, possibly different combustion regimes. Different particles arrive into the flow regions affected by turbulent mixing at different stages of their combustion. The precise instant when each particle becomes affected by turbulent mixing depends on at least two

parameters: particle size and its axial coordinate. Larger particles tend to have longer pre-heating times compared to smaller particles; particles located further away from the jet's center tend to ignite sooner compared to the centrally located particles because of greater oxidizer availability. Neither particle size nor its exact axial location could be measured directly, thus meaningful analysis of the respective data where the ''laminar'' and ''turbulent'' burn rates are separated from each other was impossible. Instead, of interest here is the gross effect of turbulence on the statistically distributed burn times of metal particles, which is addressed in the present experiments.

The flow configuration achieved in the experiment is analogous to that of a fireball produced by a metalized explosive and expanding in air [42]: turbulent mixing of the fireball with its surroundings affects both flow pattern and gas composition to which the metal particles within the expanding fireball are subjected. The gross effect of this turbulent mixing on the particle combustion rate is of substantial interest, and the effect is examined here in a laboratory experiment.

2.2 Powder Feeder

A custom screw feeder (Figure 2.2) described in more detail elsewhere [35, 39] was used to feed the metal particles into the burner. To coat the screw with powder, the dry powder was placed in a plastic dish and weighed. Using a short bristle brush, the powder was deposited into the threads of a stainless steel, ¾" (19.05 mm) diameter screw with 16 threads per inch. A typical powder load was 0.1 g, which was placed over about 7-cm length of the screw. Prior to coating the powder onto the screw, the powder mass was measured. After the powder had been applied, the remaining weight was also recorded to determine the sample mass to be used in

experiments. The screw loaded with powder was then placed into a cylindrical enclosure and attached to a DC-motor. A narrow nitrogen jet blowing across a thread of the loaded screw removed powder coating and fed it into the burner. The feed rate of powder was determined by the rotational speed of the screw. It was pre-selected in preliminary experiments to ensure production of as many particle streaks as possible during the data acquisition time while minimizing overlapping peaks produced by multiple particles burning simultaneously.

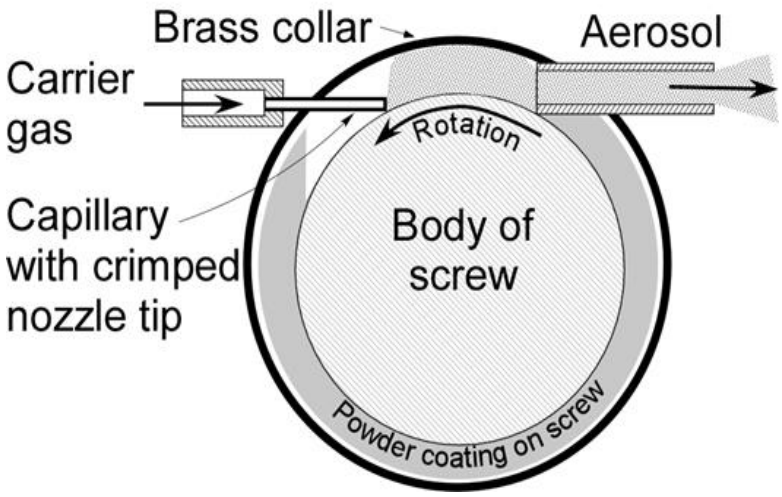

Figure 2.2 Schematic diagram of powder feeder.

Sources: Amy Corcoran, Stefano Mercati, Hongqi Nie, Massimo Milani, Luca Montorsi, and Edward L Dreizin "Combustion of fine aluminum and magnesium powders in water" New Jersey Institute of Technology. Combustion and Flame 160(2013)2242-2250.
www.elsevier.com/locate/combustflame.

2.3 Burner

A schematic diagram of the steel burner and enclosure used to generate turbulent flow patterns is shown in Figure 2.3 Acetylene and air are fed through a tube with narrowed internal diameter. Fine brass screens were installed to enhance mixing. A thin stainless steel tube placed at the axis of the burner was used to inject the particles carried by nitrogen. The flame shape is sensitive to the position of the central tube, which must be carefully centered to achieve the desired symmetric flame configuration. The produced flame is laminar. To generate turbulence, the flame needs to be disturbed or agitated. This is achieved by directing three tangential air jets around the flame to produce a swirling flow. The burner is equipped with an attachment including three nozzles directed tangentially inside a hollow cylindrical enclosure. The enclosure and one of the nozzles are shown in Figure 2.3. The burner is placed inside the cylinder, and the air flow is adjusted to create the desired level of turbulence. Individual rotameters are used to monitor air, acetylene, and air flow rates.

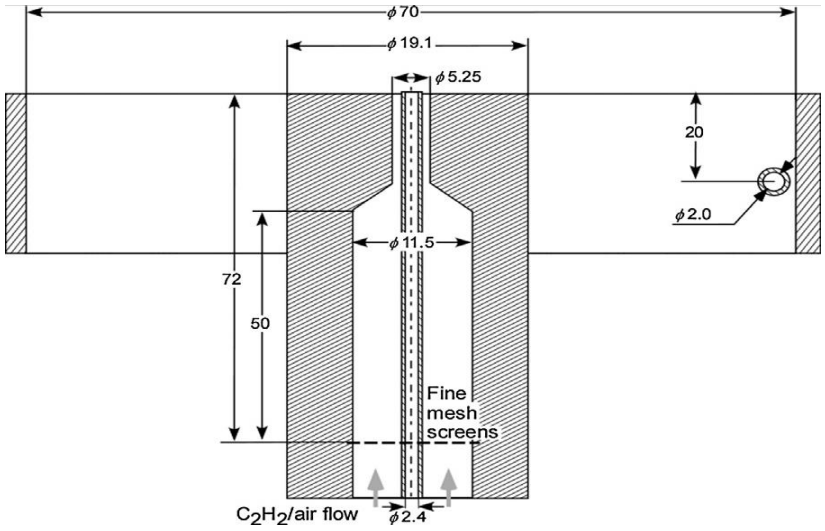

Figure 2.3 Schematic diagram of the burner together with enclosure and one of the turbulence-generating nozzles and all dimensions are in mm.
Sources: Amy Corcoran, Stefano Mercati, Hongqi Nie, Massimo Milani, Luca Montorsi, and Edward L Dreizin "Combustion of fine aluminum and magnesium powders in water" New Jersey Institute of Technology. Combustion and Flame 160(2013)2242-2250.
www.elsevier.com/locate/combustflame.

2.4 Material

Two spherical magnesium powders provided by Hart metals, Inc., were used. One of the powders was described by the manufacturer as Magnesium-325-Mesh, and the other nominally contained particles with sizes in the range of 1-11μm. As discussed below, it was observed that the 1-11 μm powder had a thicker effective oxide coating than the other. In order to verify the effect oxide thickness, the -325 Mesh powder was subjected to a controlled aging. Two aged powders were prepared. In one experiment, the powder was placed in a furnace (53L 250°C Vacuum Oven (16x13x14) With 28 Segments Temperature Controller - EQ-DZF-6050 series) at the temperature of 50 °C (323 K) for 72 hours. Separately, the same powder was subjected to a heating program in a sample holder of TAM III (a micro-calorimeter by TA Instruments) in a flow of mixed oxygen (10%) and argon (90%) with the total flow rate is 50 ml/hour. The temperature increased from 25 to 145 °C with the heating rate of 2 °C/hour.

All powders were characterized using scanning electron microscopy (SEM). For SEM analyses, a Phenom Tabletop microscope by FEI Technologies Inc., as well as LEO 1530 Field Emission Scanning Electron Microscope were employed. Secondary electrons were used to obtain images.

Particle SEM images for both -325 Mesh powders and 1-11 μm powders are shown in Figure 2.4. Nano-sized oxide particles are observed to adhere to the Mg surface for both powders, more such particles appear to cover the surface of the finer, 1 – 11 μm particles compared with the coarser, -325 Mesh powder. For coarse powder, almost all particles are spherical. For fine particle, most particles are also spherical; however, coalesced spheres and non-spherical particles are also observed.

Close-up SEM images for both as received and "aged" powders (-325 Mesh) are shown in Figure 2.5. The aged particles shown have been subjected to 72-hr heating at 50 °C. Qualitatively similar surface features were observed for the particles aged in the sample holder of TAM III. "As received" powders have smooth surface decorated, as noted above, with small crystalline particles, likely MgO. Aged particles retain the spherical shapes. For "aged" particles, the surface appears to develop light-colored inclusions, which are likely representative of the heavier oxidized areas.

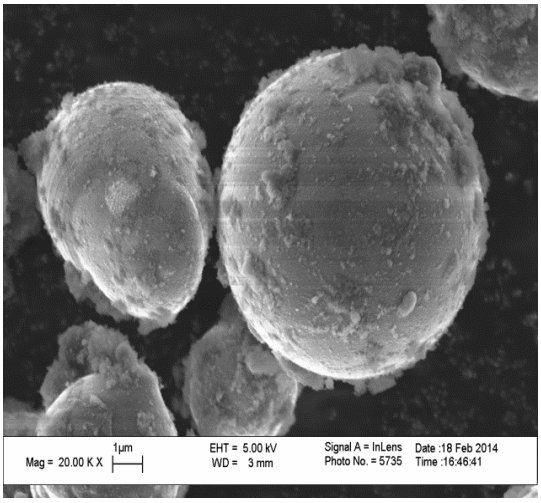

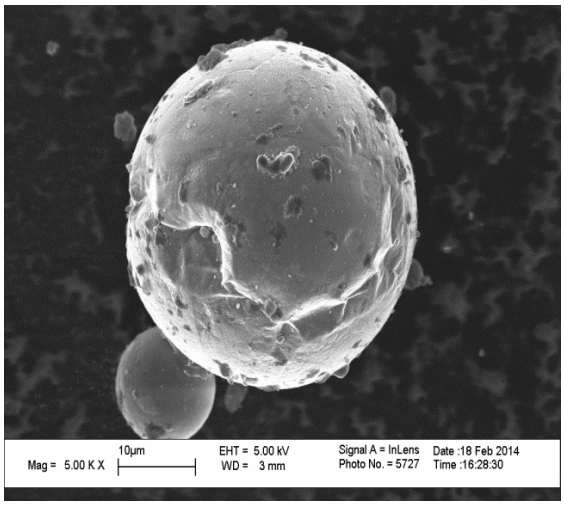

Magnesium 1-11um powder Magnesium -325 Mesh powder

Figure 2.4 SEM images of the commercial Mg powders used (secondary electron images).

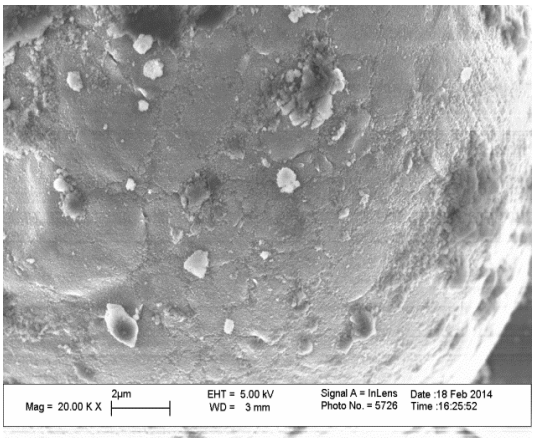

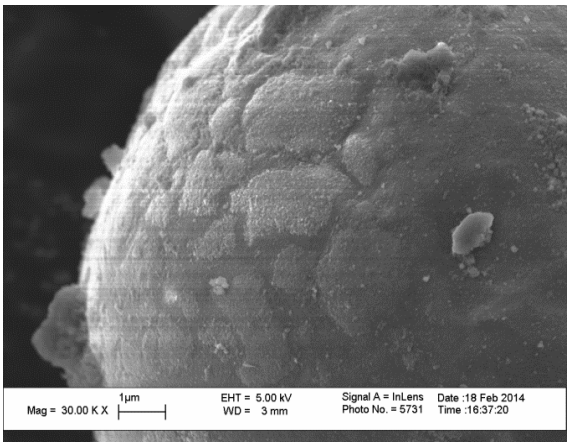

Magnesium -325 Mesh as received powder Magnesium -325 Mesh aged powder

Figure 2.5 SEM images for as received and aged powder, -325 Mesh.

Particle size distributions for all powders were measured using a Beckman-Coulter LS230 Enhanced Particle Analyzer and are shown in Figure 2.6 for both as-received powders. The particle size distribution for both aged and as received -325 Mesh powders are compared to each other in Figure 2.7. Aging did not apparently affect the particle size distribution and minor

discrepancies between the two histograms shown in Figure 2.7 are comparable to those observed for repeated measurements for the same powder.

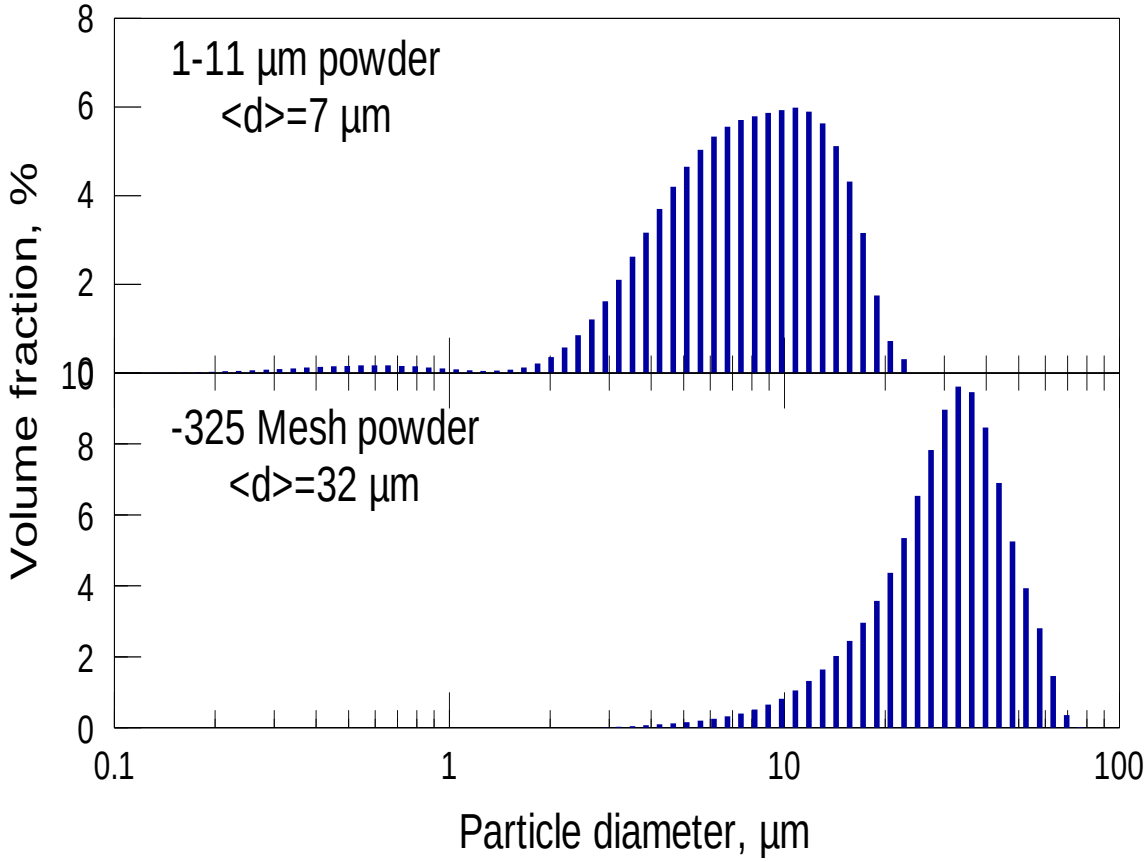

Figure 2.6 Particle size distribution for the magnesium powders used.

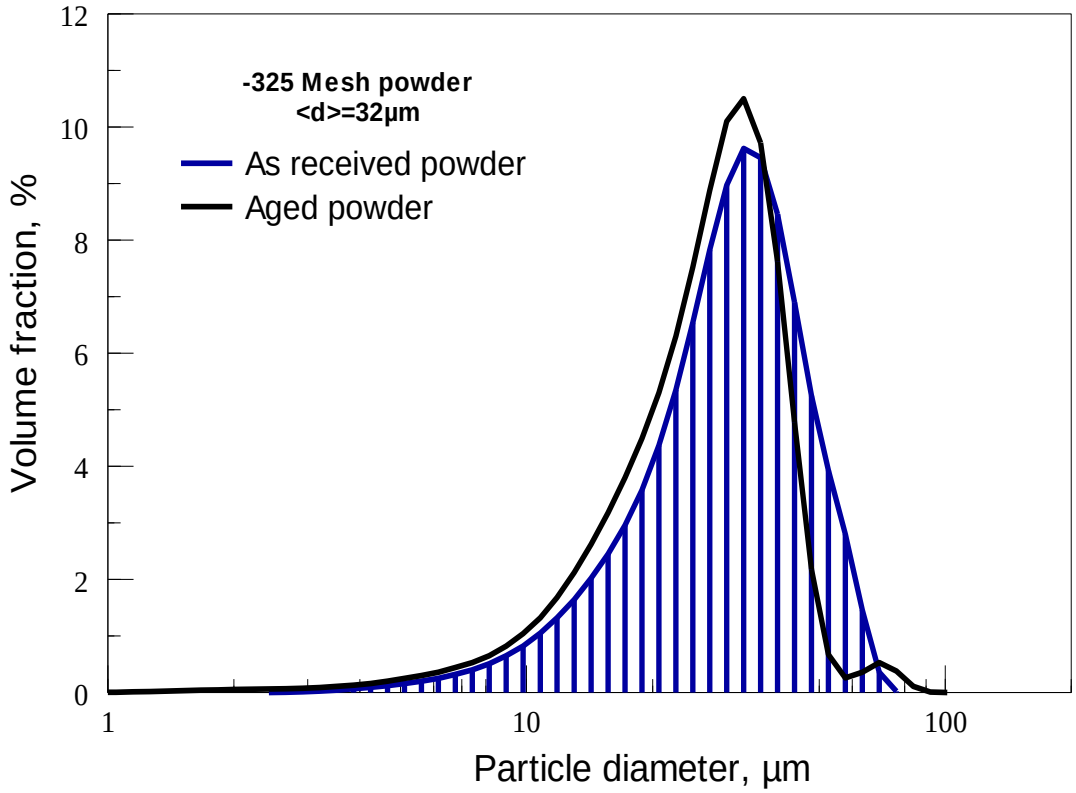

Figure 2.7 Particle size distribution for both aged and received powders.

Many very fine particles, less that 1 µm, were appearing on the size distributions obtained by the Beckman-Coulter LS230 Enhanced Particle Analyzer for the 1-11 µm powder, as shown in Figure 2.6. However, such particles were unexpected based on the manufacturer's specification. It was suspected that the submicron sized particles are either an artefact of the measurement or could represent separated nano-sized oxide particles adhering to the surface of spherical Mg, as seen in Figure 2.4 which could be knocked off the surface by ultrasonic agitation used during the measurement. To verify the presence or absence of submicron size particles, several optical microscope images with multiple particles in the field of view were taken and examined. An example of such an image is shown in Figure 2.8. Particles with the diameter smaller than 1.2 µm were not detected (images with different focusing conditions were

taken with the reproducible final results, as shown in Figure 2.8), which agrees with the manufacturer's specification.

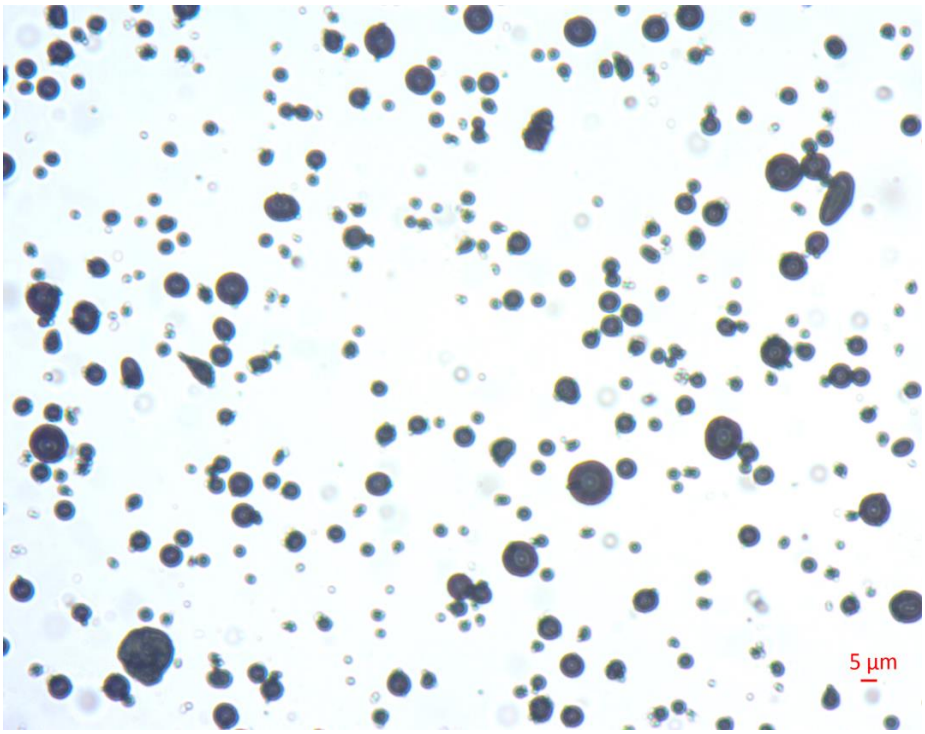

Figure 2.8 Powders are observed under electron microscopy.

Respectively, the measured particle size distributions were corrected by removing the fraction representing the ultrafine particles. The remaining particle size distribution was re-normalized to represent 100% of the particles. For processing experimental data, both as measured and corrected re-normalized particle size distributions were used. Note that no correction was required for the -325 Mesh powder.

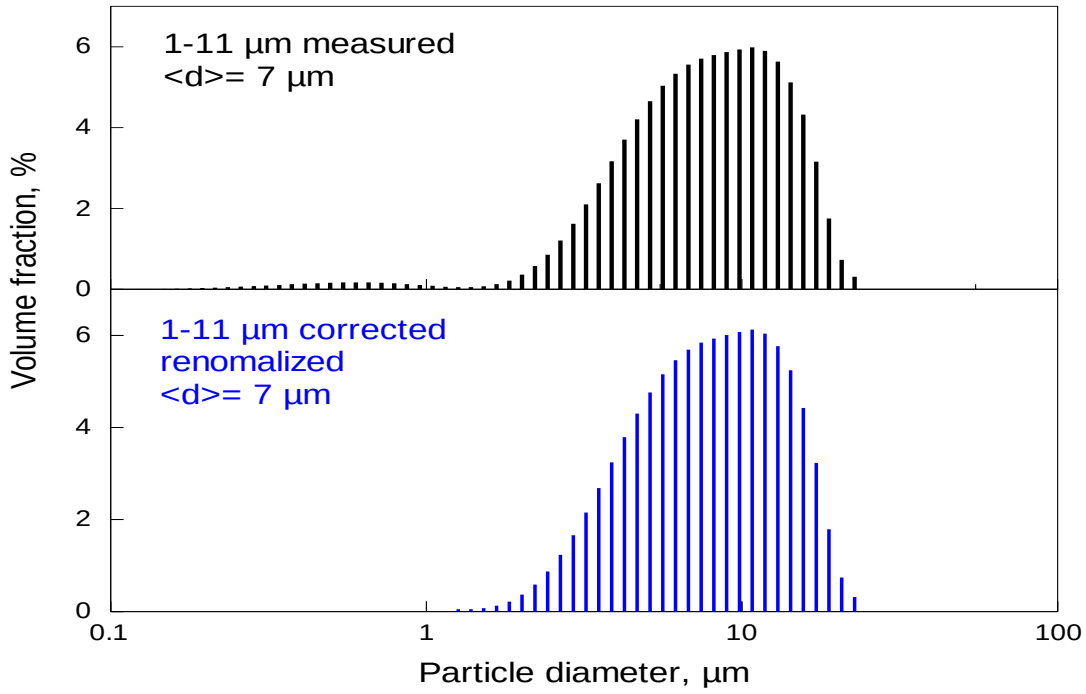

Figure 2.9 As measured and corrected and renormalized particle size distribution for magnesium 1-11µm powder.

2.5 Data Acquisition and Processing

2.5.1 Data Acquisition

Among the three PMT's used to record emission of the burning particles, two were Hamamatsu R3896-03 equipped with 700 and 800-nm interference filters, and the third, Hamamatsu R636-10 was equipped with a 900-nm interference filter. A fiber optics bundle connected to the PMT array was placed about 13 cm away from the burner. This placement produced optimal results for capturing emission from entire particle streaks while minimizing the noise produced by the flame. The PMT outputs were recorded and saved at a rate of 100,000 samples per second using a 16-bit PCI-6123 data acquisition board by National Instruments and Lab-view software. The range of voltages recorded was from 2 to 5 V, which resulted in a 0.306 mV signal resolution. The signal changes within ±5 times of this resolution value were considered to represent the level of digital noise. The data were processed using a custom Matlab code.

The signals from the PMT's were recorded and processed with two objectives:

1. To obtain the burn times of individual particles, and find a correlation between the burn times and particle sizes.

2. To quantify the burning particle temperatures.

2.5.2 Identifying Particle Emission Pulses

A characteristic example of the signal recorded by one of the PMT's is shown in Figure.2.10. The signal includes a substantial background produced by emission from the hydrocarbon flame. Despite the background emission, peaks produced by the burning Mg particles can be reliably identified. In addition to the peaks produced by individual burning particles, inevitably some peaks produced by combustion of several particles burning simultaneously were recorded. A three-step procedure was developed for semi-automated processing the recorded signals and selecting the emission peaks generated by individual particles for further analysis.

In the first step, the signal level representing the baseline background flame emission was selected. The average signal value was determined with averaging over 100 points, representing 1ms. The baseline signal was identified when short term signal changes have not increased or decreased by more than 5 times the signal resolution, which represented 1.53 mV.

In the second processing step, peaks produced by burning particles were selected. For each portion of the signal exceeding the baseline by more than the pre-set threshold level for more than 5 points acquired in a continuous sequence, a peak was identified. The threshold level was selected to be 5 times the signal resolution.

Finally, in the third processing steps all identified pulses were analyzed and filtered to remove those representing multiple burning particles. All pulses, for which the signal did not start from or return to its initial baseline level and remained there for at least 5 recorded time

steps were filtered out. In addition, pulses showing multiple peaks of comparable amplitude were filtered out.

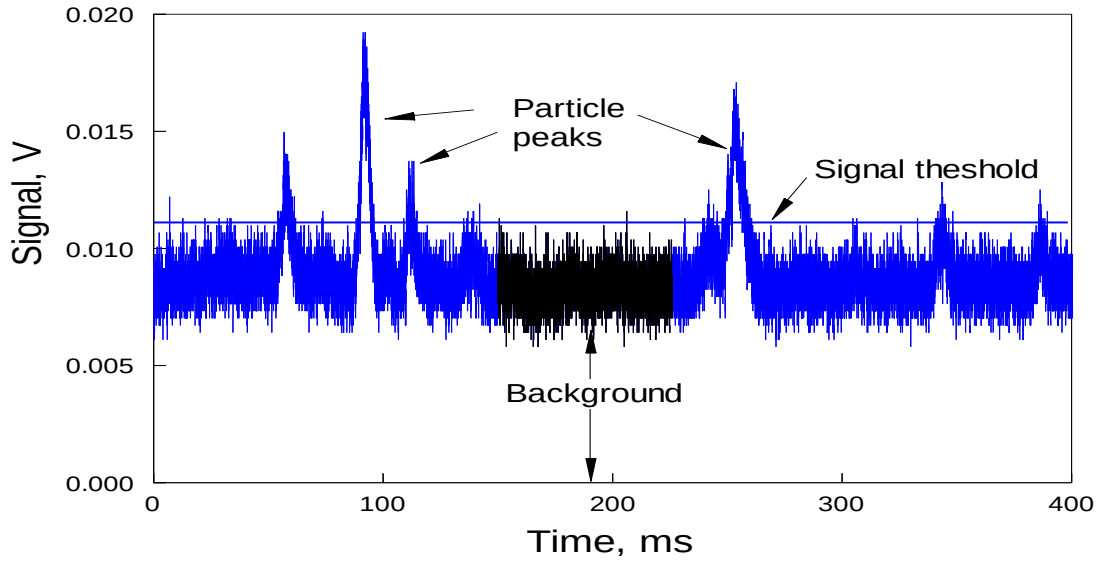

Figure 2.10 Magnesium particle combustion signals with selected baseline, threshold and starting point

After the particle peaks were selected, an additional processing step was used to remove possible outliers, which may not have been captured by the processing described above. It was expected that the larger size particles would generate emission peaks that are both longer and greater in the amplitude, compared to the smaller particles. In other words, a direct proportionality between the particle peak amplitude and duration was assumed. Indeed, a direct proportionality trend is observed in Figure 2.11 showing pulse amplitudes plotted against their durations for two recorded data sets for the two Mg powders. Each open symbol represents an emission pulse identified by the processing described above.

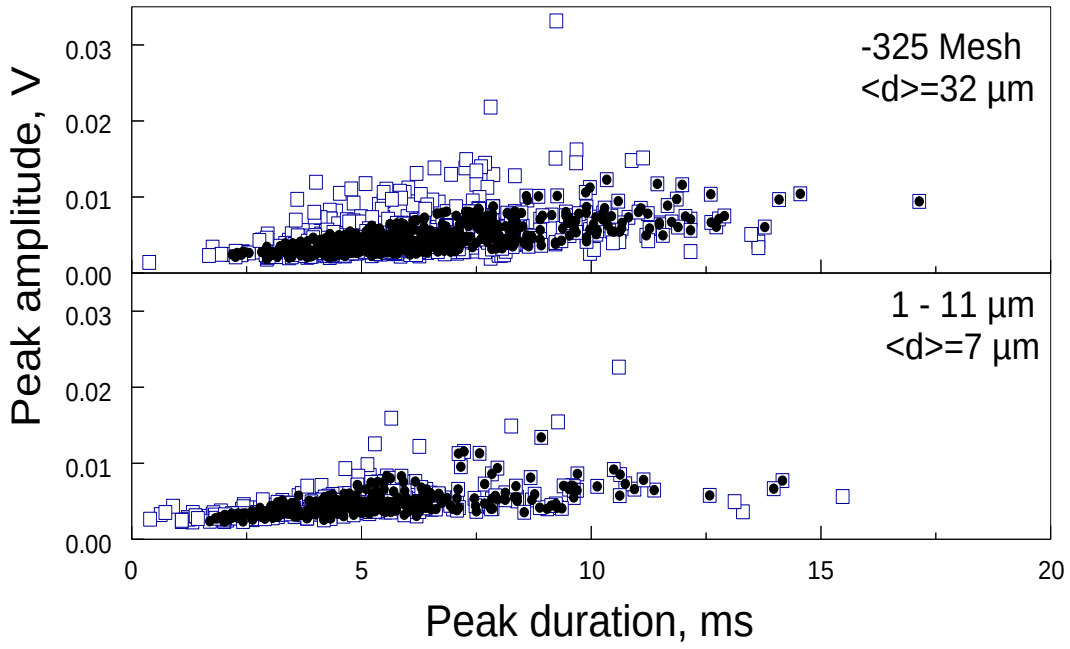

Figure 2.11 Peak amplitude versus peak duration.

A MATLAB code was prepared that processed all the identified particle peaks and characterized each peak by a number representing its amplitude to duration ratio. For example, a statistical distribution of the obtained amplitude to duration ratios for a selected experiment is shown in Figure 2.5.1. For this example, the most common ratio is 0.7 mV/ms, which represents the average slope for the trend line based on the points shown in Figure 2.11 Although the obtained histogram shows a clear peak, there are many recorded pulses for which the amplitude to duration ratios is substantially different from the most common values. Typically the pulses with amplitude to duration ratio outside of the half width of the histogram peak were considered as outliers. Such pulses are represented by color bars in Figure 2.12 The pulses left for the final analysis, after the outliers were removed, are shown as filled

symbols in Figure 2.11. Filled symbols represent a large subset of the open symbols, which include both pulses left for analysis and outliers.

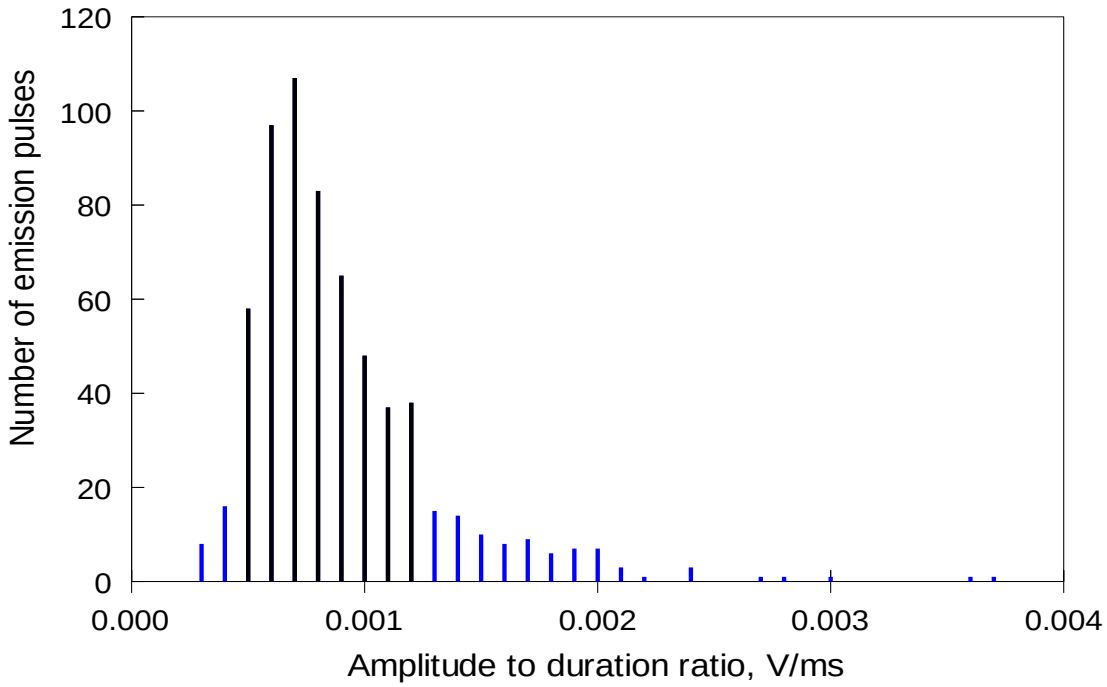

Figure 2.12 Number particles per bin versus bins.

It is apparent that the selected pulses form a tighter linear trend. However, the trend line for both filled and open symbols is apparently the same. To verify validity of this last processing step, the assessment of burn times as a function of the particle sizes was performed for both the complete pulse set and the pulse set with removed outliers.

2.5.3 Burn Time Measurement

A correlation between particle burn times and particle size distribution was obtained using the experimental data. A distribution of pulse durations was obtained processing data from all down selected particle emission pulses for each experiment with a specific Mg powder burning

with a specified flame flow configuration. An example of such a cumulative distribution is shown in Figure 2.13. Assuming, that the larger particles burn longer, the distribution of pulse durations was directly correlated with the distribution of particle sizes, shown in Figure 2.15. Both directly measured and corrected particle size distributions were considered. To make a direct correlation, data from Figure 2.13 were re-plotted as a cumulative distribution for number of particles, as shown for example in Figure 2.14.

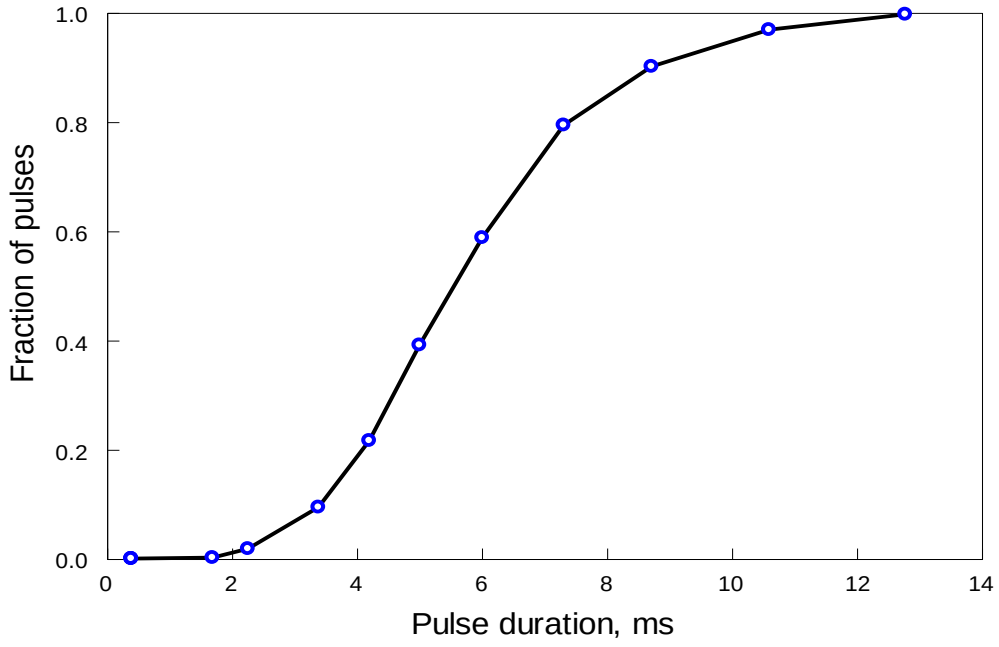

Figure 2.13 Cumulative distribution of pulse durations measured in a specific data set for -325 Mesh powder burning in a laminar flame.

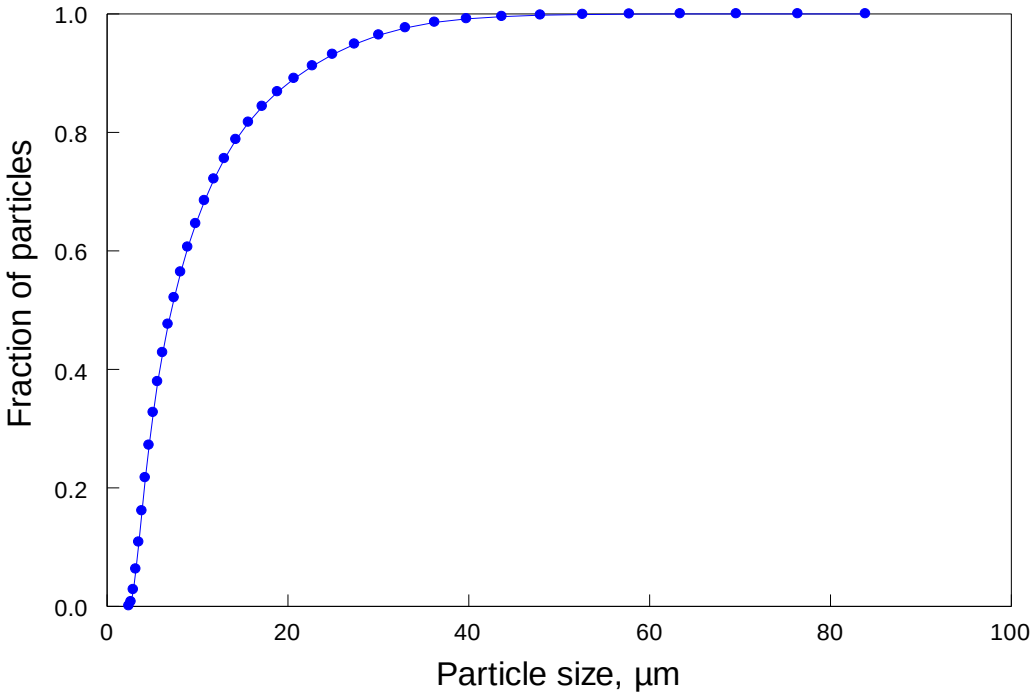

Figure 2.14 Cumulative distribution of particle sizes for -325 Mesh powder.

For each pulse duration bin, representing a specific fraction of particles, a respective particle size was identified considering the same fraction of particles for the particle size distribution. The particle size was obtained by interpolating between respective particle sizes considering the closest size bins in the size distribution. An example of the obtained correlation is shown in Figure 2.15. As discussed below, a very strong apparent effect of particle size on the burn time for the finest particles is superficial and disappears when the outlier points (cf. Figures 2.11 and 2.12) are removed from the analysis.

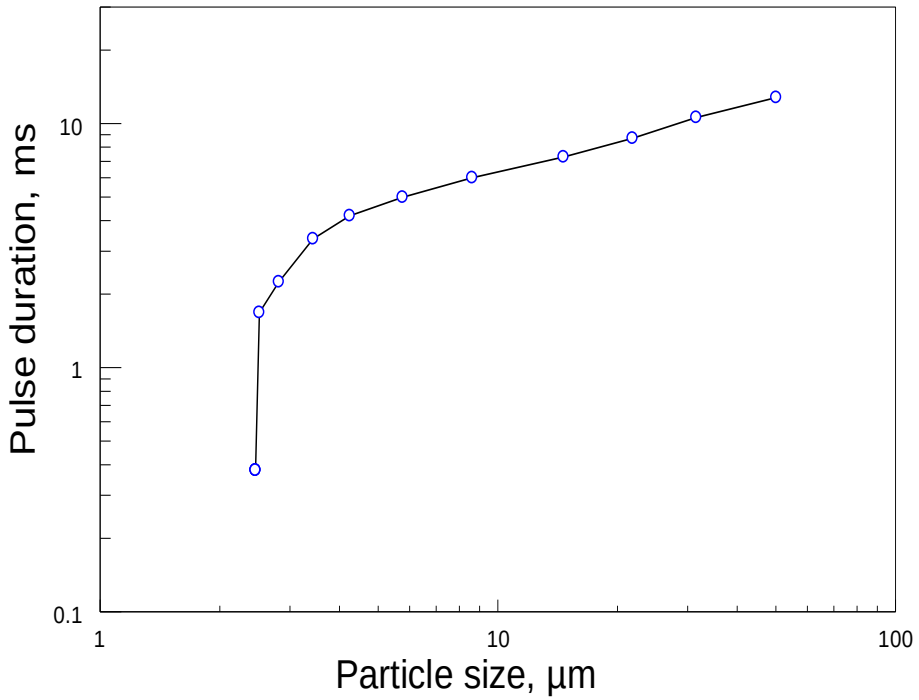

Figure 2.15 Particle burn times versus particle sizes obtained correlating data from Figures 2.13 and 2.14.

Correlations similar to that shown in Figure 2.15 were obtained for data sets representing different powder samples burning in different flow conditions. These were considered to represent the burn times as a function of the particle size.

2.6 Temperature Measurements

2.6.1 General Approach

The optical emission traces produced by the burning particles were recorded at three wavelengths. The ratios of the recorded traces were used to determine color temperatures of the burning particles. To obtain the temperature measurements, it was necessary to calibrate the outputs of the filtered PMT's. Each PMT was equipped with an individual high voltage power source. The high voltage was adjustable enabling one to select the proper sensitivity for each filtered PMT. The adjustment is monitored by a low voltage value, so called monitor voltage,

which is directly proportional to the high voltage applied to the PMT. The calibration for the temperature measurements was performed for a range of PMT voltages, and, respectively, for the range of their monitor voltages. A StellarNet spectrometer EPP-2000 was first calibrated and used as a reference device for the calibration of PMT outputs.

2.6.2 Calibration of the Spectrometer

A halogen tungsten lamp fed by a regulated DC power supply was used as a source of emission for the PMT calibration. A StellarNet spectrometer EPP-2000, SpectraWiz software was used as a reference source generating a gray body spectrum based on the tungsten lamp emission. First, the calibration for the spectrometer was corrected using a calibrated source lamp LS-1-CAL by Ocean Optics and the lamp calibration data file. Parameters for data acquisition and processing were selected, the fiber optics cable was connected to the spectrometer and the spectrometer was connected to the USB port of a data acquisition computer. The LS-1-CAL lamp was aligned with the front end of the fiber optics cable connected to the spectrometer. The distance between the lamp and the fiber optics cable was 25 cm. In the Spectra-Wiz software, a 'Watt' button was pressed and a Cal file was saved. Immediately after saving the Cal file, a dark reading is prompted and taken with the lamp turned off. The laboratory is dark during these measurements.

2.6.3 Acquiring Calibrated Spectra using a Halogen Tungsten Lamp

Emission spectra of the halogen tungsten lamp (36W, 12VDC nominal voltage) were acquired at different currents supplied to the lamp in the visible wavelength range. The spectra were collected using StellarNet Spectrometer EPP-2000 and SpectraWiz software. The lamp was fed by a regulated DC power supply. Neutral density filters by Edmund Optics (optical densities

from 0.5 to 3.0) were used to extend the range of the lamp temperatures covered by the measurement.

The tungsten lamp was aligned with an optical filter (if necessary) and the spectrometer fiber optics cable. The distance between the optical fiber inlet and the lamp was selected in the range of 15 - 25cm. The DC power supply was connected to the tungsten lamp and the desired current level was set. The power supply was used in the current control regime. Without turning on the power supply, a dark spectrum was taken using the SpectraWiz software. The dark spectrum must be taken every time the parameters of the spectrum acquisition are changed. To collect an emission spectrum, the power supply was turned on, and about 10 seconds was allowed for the halogen lamp to achieve a constant brightness. The spectrum was then taken and saved. For each current level, it was verified that the spectral intensity is not saturated for any wavelengths. If the signal was saturated, a neutral density filter was used and the measurement was repeated. For each acquisition, the software was switched into 'Watts' mode, the signal was acquired and saved. The measurements were repeated for various currents, to capture a broad range of the halogen tungsten lamp temperatures.

2.6.3 PMT Calibration

For each setting of the tungsten halogen lamp, corresponding to a specific temperature, PMT signals were collected at various monitor voltage values. The fiber optics cable connected to the filtered PMT's was aligned with the halogen tungsten lamp. A distance between the fiber optics cable and the lamp was chosen in the range of 3 – 8 cm. To avoid blinding and destroying the PMT's, all the lights should be turned off when working with the PMT signals. The power supply voltage connected to the high voltage PMT power supply was set to 12 V. The power on the regulated DC power supply connected to the halogen tungsten lamp was turned on; the

maximum current was set at 2.0A. The monitor voltage for each PMT channel was selected using a digital voltmeter. The monitor voltage was varied from 2 to 5 V with a 0.l V step. The measurements were taken at various tungsten lamp powers, adjusted using the regulated power supply. A typical step size while adjusting the tungsten lamp power was 0.2 A. The maximum current was limited to 6 A.

2.6.4 Temperature Calibration for the Filtered PMT's

A calibrated spectrometer output for each tungsten lamp's current was obtained. A typical spectrum is shown in Figure 2.16. Such spectra were curve-fitted using Plank's equation, corrected by the tungsten emissivity, ε_λ:

$$I_\lambda(T) = \varepsilon_\lambda \frac{2hc^2}{\lambda^5} \frac{1}{e^{\frac{hc}{\lambda k_B T}} - 1} \tag{2.1}$$

Where T is the temperature, c is the speed of light, λ is wavelength, k_B is Boltzmann constant, and h is Planck constant. The emissivity was calculated based on experimental data [43-45] processed to obtain a polynomial fit working in the range of wavelengths of interest:

$$\varepsilon_\lambda = 0.4655 + 0.01558\lambda + 0.2675 \cdot 10^{-4} T - 0.7305 \cdot 10^{-4} \lambda T \tag{2.2}$$

The measured PMT voltage, V_λ, was assumed to be proportional to the emission intensity; the proportionality constant, k_λ was included into the curve-fitting routine, so that the final equation was:

$$V_\lambda(T) = \varepsilon_\lambda k_\lambda \frac{2hc^2}{\lambda^5} \frac{1}{e^{\frac{hc}{\lambda k_B T}} - 1} \tag{2.3}$$

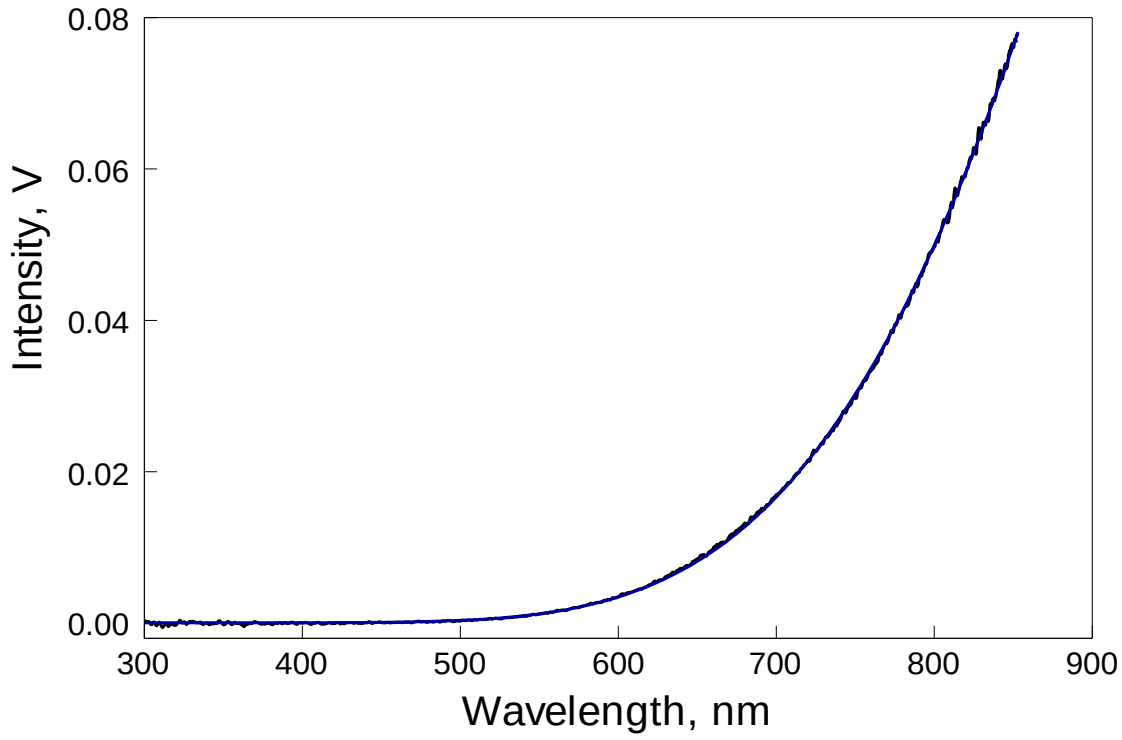

Figure 2.16 Intensity versus wavelength recorded by spectrometer.

The temperature was treated as an adjustable parameter, so that the temperature for each tungsten lamp setting could be determined. The final effect of the tungsten lamp current on the filament temperature is shown in Figure 2.17.

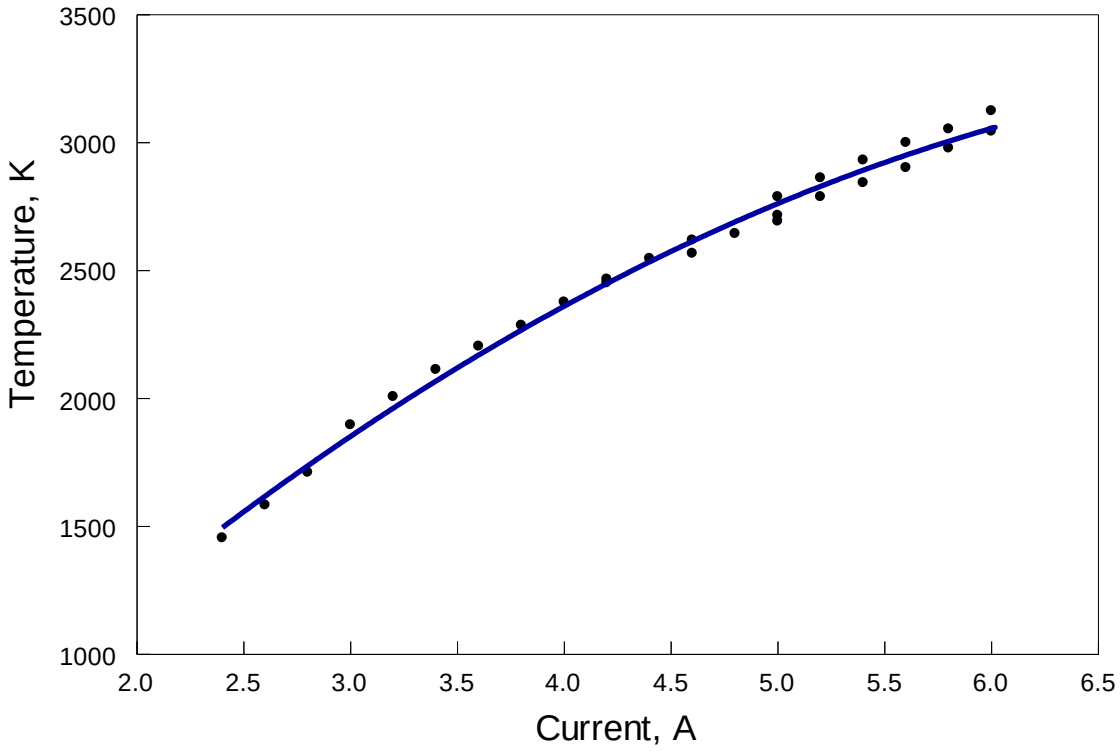

Figure 2.17 Tungsten lamp temperature versus current.

To obtain calibration for the PMT outputs for different high voltage setting, it was assumed that the output can be described by a power function relative to the high voltage applied to the PMT, or monitor voltage $V_{\lambda,m}^{n}$, so that the proportionality constant k_{λ} could be expressed as:

$$k_{\lambda} = a_{\lambda,m} V_{\lambda,m}^{n} \tag{2.4}$$

Where, constants $a_{\lambda,m}$ and n should be found for each filtered PMT channel (or for each λ used). The above assumption is based on the experimental data, such as shown in Figure 2.6.3 showing output of a PMT measured with increasing monitor voltage values, while the emission source was remaining constant.

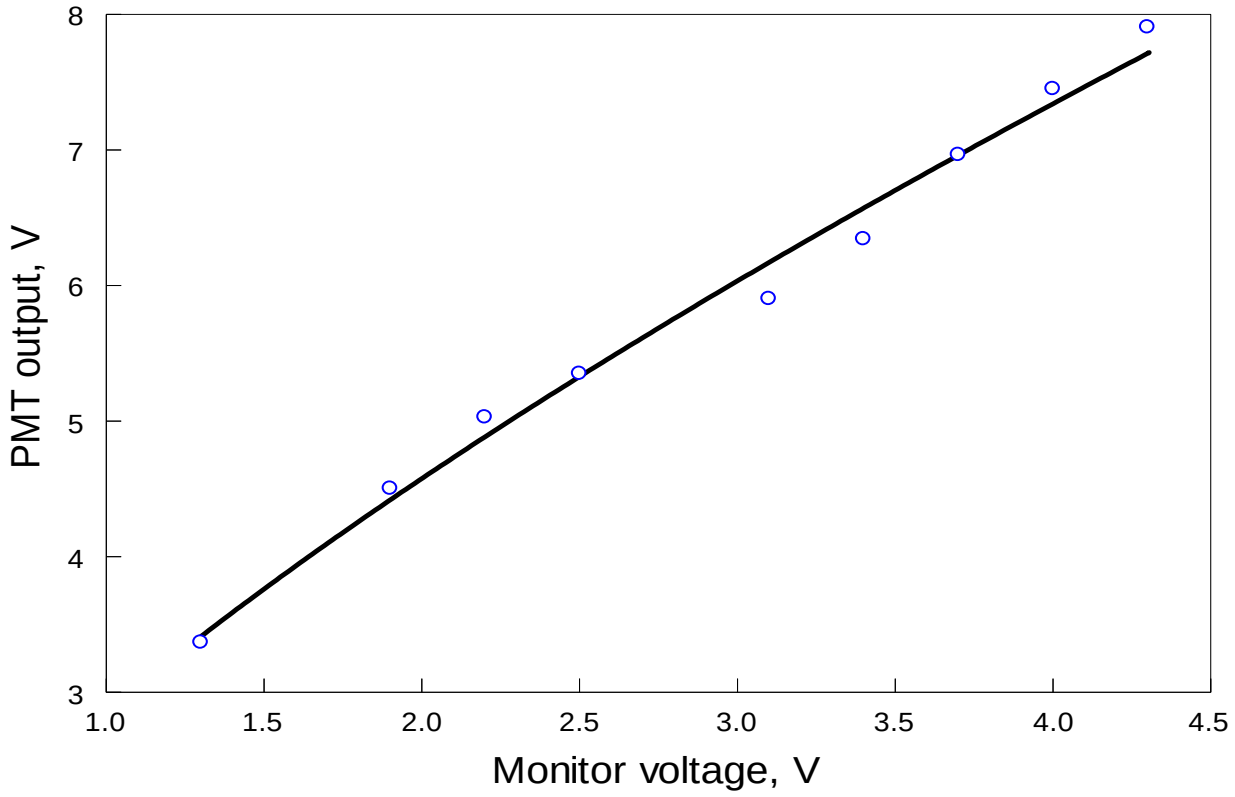

Figure 2.18 Intensity versus monitor voltage. The data are shown for a PMT filtered at 800nm. The tungsten lamp current is set at 4 A.

It is observed that for a fixed tungsten lamp setting, the output voltage V_λ is indeed described as a power function of the monitor voltage, $V_{m,\lambda}$.

Plugging Equation 2.4 into 2.3, the PMT reading could be usefully interpreted. It was observed that indeed, for each filtered PMT channel, the fixed values of constants $a_{\lambda,m}$ and n

could be found to describe the readings at different temperatures reasonably well. In practice, specific values of constants $a_{\lambda,m}$ and n were found for each setting using the curve matching; then the average values of constants $a_{\lambda,m}$ and n were selected for each channel.

Finally, a ratio of the measured voltages for different filtered channels could be considered:

$$\frac{V_{\lambda 1}}{V_{\lambda 2}} = \frac{\varepsilon_{\lambda 1} a_{\lambda 1} V_{m,\lambda 1}^{n1}}{\varepsilon_{\lambda 2} a_{\lambda 2} V_{m,\lambda 2}^{n2}} \frac{\lambda_2^{\,5}}{\lambda_1^{\,5}} \frac{e^{\frac{hc}{\lambda_2 k_B T}} - 1}{e^{\frac{hc}{\lambda_1 k_B T}} - 1} \tag{2.5}$$

After all the curve-matching parameters are found, the only unknown quantity in Equation 2.4 is temperature, T. Thus, the equation can be numerically solved for temperature and the temperature can be determined. Correlations between the measured PMT voltages and temperature are shown in Figures 2.19 and 2.20 for the ratios of different filtered PMT channel outputs. Such correlations were obtained for different values of monitor voltages and used to process the experimental data to obtain the flame temperature.

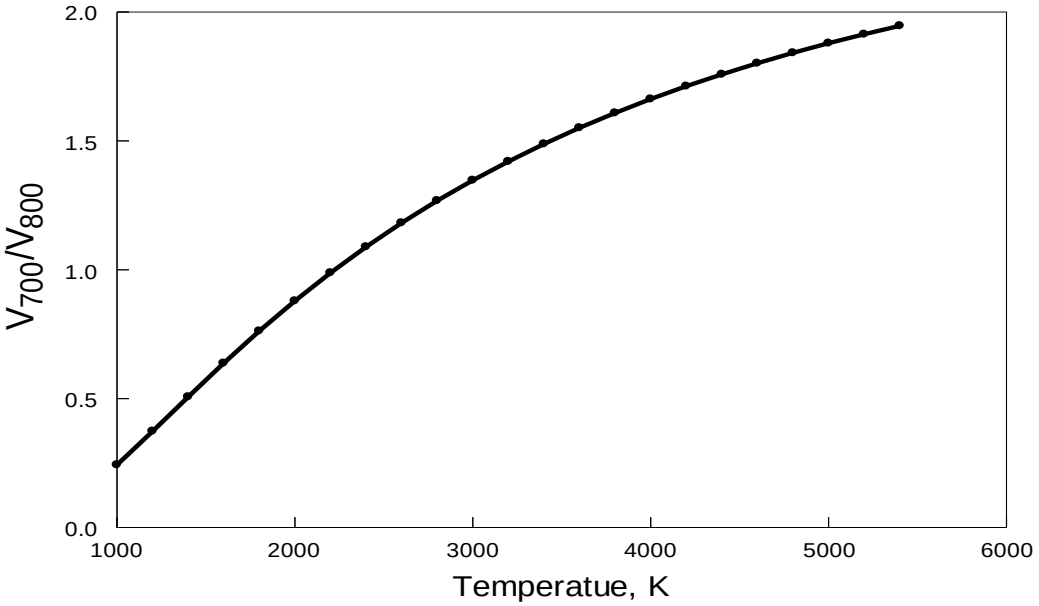

Figure 2.19 Ratio between outputs of two PMT channels filtered at 700 and 800 nm versus temperature. The data are shown for the monitor voltage of 2.2 V and 1.979 V for the PMT channels filtered at 700 and 800 nm, respectively.

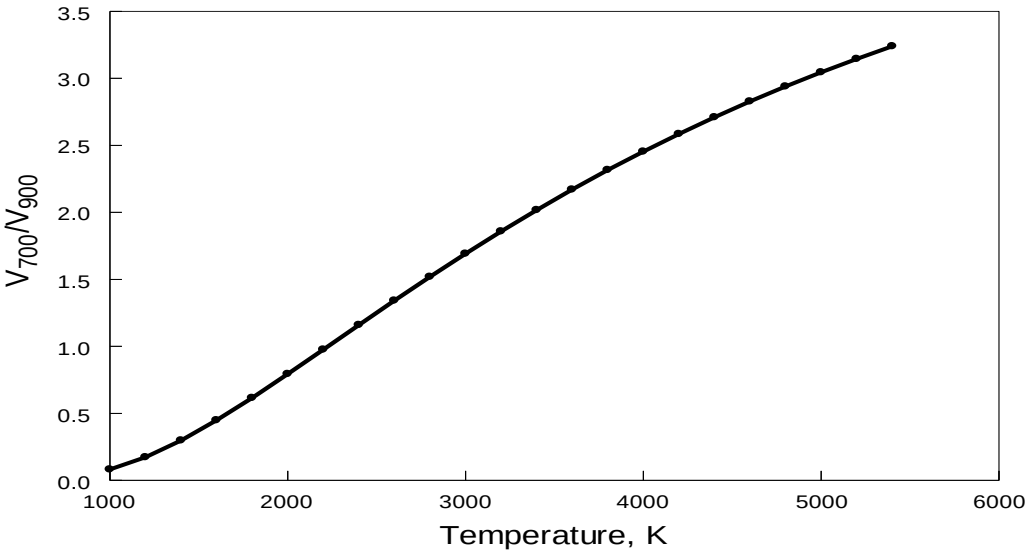

Figure 2.20 Ratio between outputs of two PMT channels filtered at 700 and 900 nm versus temperature. The data are shown for the monitor voltage of 2.2 V and 4.63 V for the PMT channels filtered at 700 and 900 nm, respectively.

2.7 Thermo-Gravimetric (TG) Study of Powder Oxidation

The main goal of this experiment was to determine the total weight gain for the fully oxidized sample and compare it to that of the starting powder to identify the effective thickness of the initial *MgO* surface coating. Both 1 – 11 μm and -325 Mesh as-received powders were oxidized. In addition, oxidation experiments were performed with the -325 Mesh powder aged by keeping it in the air at 50 °C (323 K) for 72 hours.

All powders were heated in a Netzsch STA409PG thermal analyzer using a thermo-gravimetric (TG) sample carrier with a 17-mm diameter flat corundum plate to hold the sample. The samples were oxidized in a water vapor. Oxidation in H_2O was used because it results in a complete oxidation of the Mg powder at a temperature lower than that for oxidation in oxygen. Thus, the undesirable effect of magnesium sublimation during the experiment is minimized.

The sample was heated at 10 K/min. The furnace was connected to a pressurized boiler, which was held at 453 K. The connecting lines were heated to temperature 423 K to prevent condensation. Argon was introduced into the furnace in two locations. The first invariant gas flow of 50 ml/min serves to protect the thermo balance from any condensation. It enters the furnace from below. Due to the furnace geometry, it has a negligible contribution to the atmosphere that the sample is exposed to. The second argon flow at 5 L/h (83.3 ml/min) was used as a carrier gas for steam, entering the furnace from above. The steam flow rate was 0.92 g/h at the boiler temperature, resulting in an atmospheric composition of 20 volumetric percent of H_2O.

CHAPTER 3

RESULTS

3.1 Presence of Initial *MgO* Layer

Thickness of the initial MgO coating was evaluated for all powders used in combustion experiments. First, the measurements were performed for both as received powders with the manufacturer-specified particle sizes of 1-11 μm and -325 Mesh. Results of these measurements are shown in Figure 3.1.

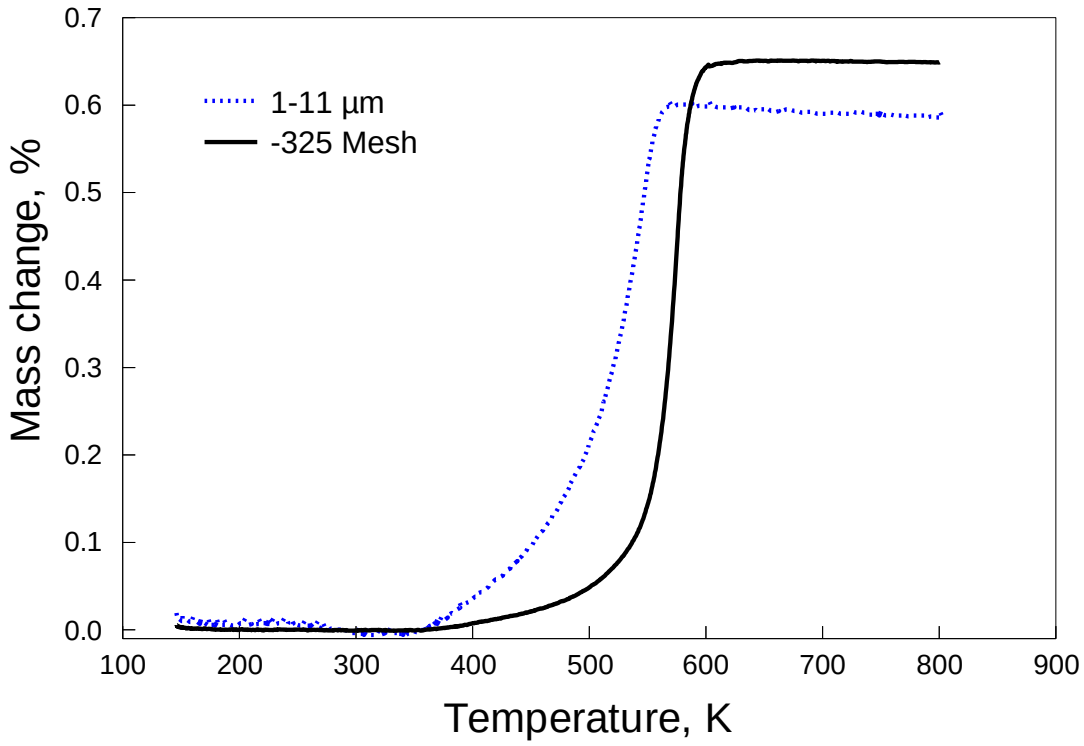

Figure 3.1 Weight increase for the 1-11 μm and -325 Mesh powders oxidized in water vapor with heating rate of 10 K/min.

It is observed that the total weight increase is greater for the -325 Mesh powder, indicating that this powder is less oxidized as received.

The weight increase was also compared for the aged and as received powder (-325 Mesh). The resulting TG curves are shown in Figure.3.2. The weight increase is slightly greater for the powder as received, indicating that that powder was less oxidized, as expected.

The effective thickness of the oxide layer, θ, was estimated based on the measured total weight increase, Δm,

$$\theta = r[1-(\frac{1}{1+\frac{\rho_{mg}}{\rho_{mgo}}(\frac{M_O}{M_{mg}}\frac{m_o}{\Delta m}-1)})^{1/3}] \tag{3.1}$$

Where, r is the average particle radius, obtained from the particle size distribution (Figure 2.6 – Figure 2.9), m_0 is the initial sample mass loaded in the TG, M_O and M_{Mg} are molecular weights of oxide atom and magnesium, respectively, and ρ_{MgO} and ρ_{Mg} are densities of magnesium oxide and magnesium, respectively.

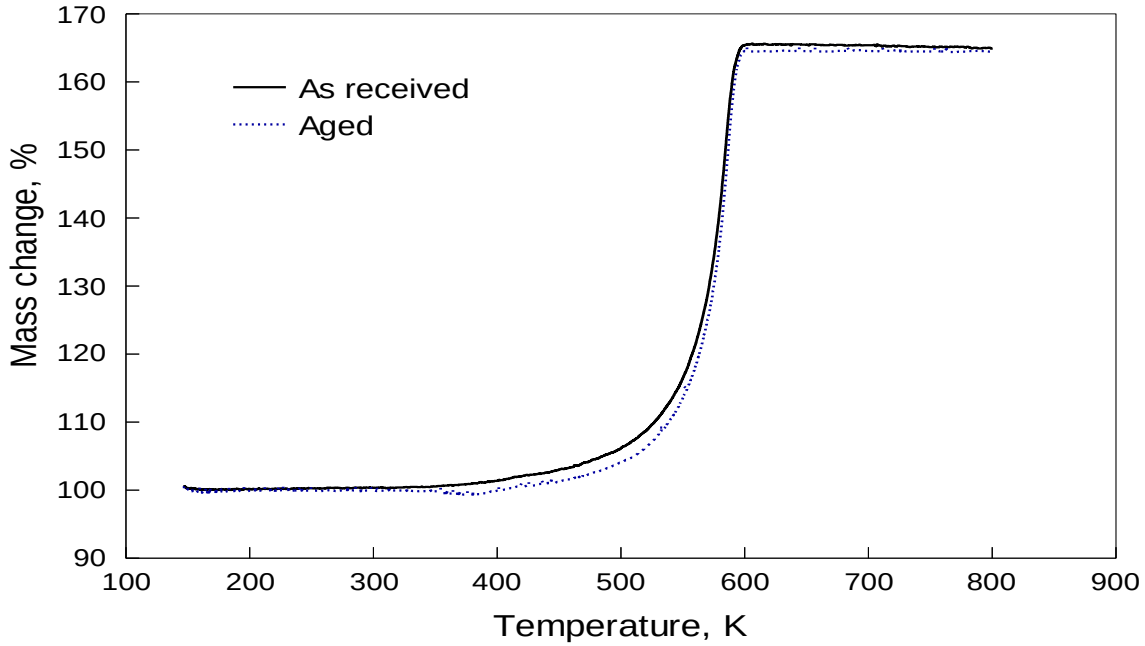

Figure 3.2 TG curves for as received and aged powders, -325 Mesh.

The results of calculations of the initial oxide thickness for different powders are shown in Table 3.1.

Table 3.1 Initial Oxide Thickness for Different Mg Powders Determined from Processing TG Traces

Powders	As received powder		Aged powder
	1– 11 μm	-325 Mesh	-325 Mesh
Average, surface area based particle radius, *r*, μm	3.4	12.5	12.5
Effective oxide thickness, nm	45	24	44.8

The difference in the effective oxide thickness between two as-received batches of Mg powder is not negligible. This difference is close to that between as-received and aged -325 Mesh powders. This difference, as discussed below, may be responsible for the different burn times observed for particles of the same sizes from different Mg powder batches.

3.2 Appearance of the Flame and Combustion Products

Multiple images of the ignited particle streaks were taken for different levels of turbulence as illustrated in Figure 3.2. There was no apparent difference in the flame shape, particle streak

length or color when different powders (as received 1 – 11 μm, -325 Mesh, or aged -325 Mesh) were used.

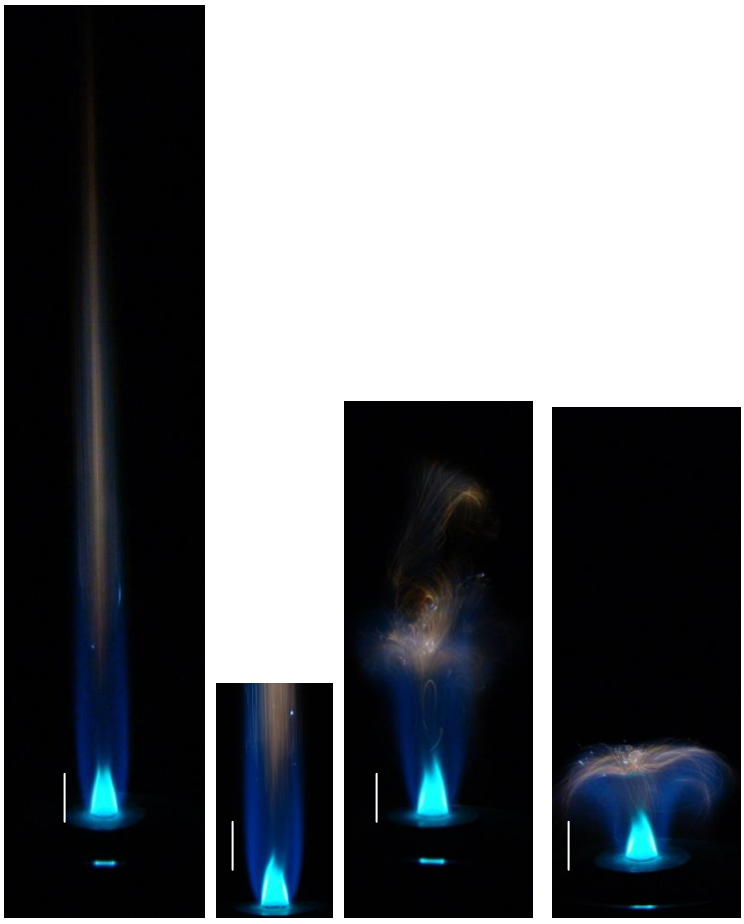

Figure 3.2 Images of flame for different turbulent levels and the scale bars in the three images are 1.5 cm each.

For laminar flow, the flame is extended in the vertical direction. The particles are observed to ignite at about 3-4 cm from the burner exit. The streak lengths vary from 15 to 22 cm. The velocity of the combustion products is estimated to be 19.32 m/s. As the turbulence-inducing flows are added, particle streaks appear to curve more and more. The lengths of the streaks reduce markedly. However, the ignition point appears to remain relatively constant for all turbulence levels.

SEM images of the combustion products collected from the flame are shown in Figures 3.3 and 3.4.

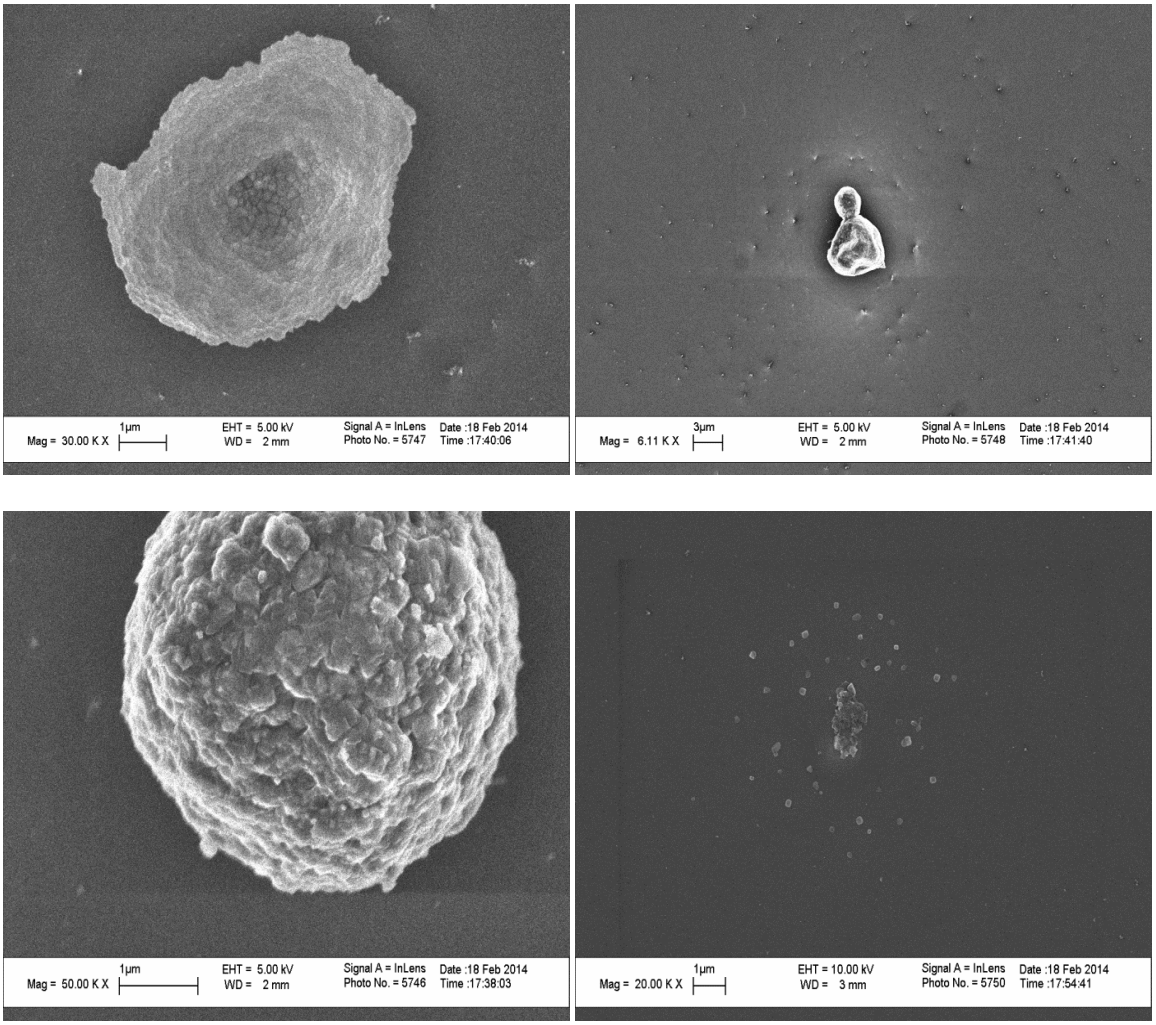

Figure 3.3 SEM images of combustion products of the -325 Mesh powder collected from air-acetylene flame.

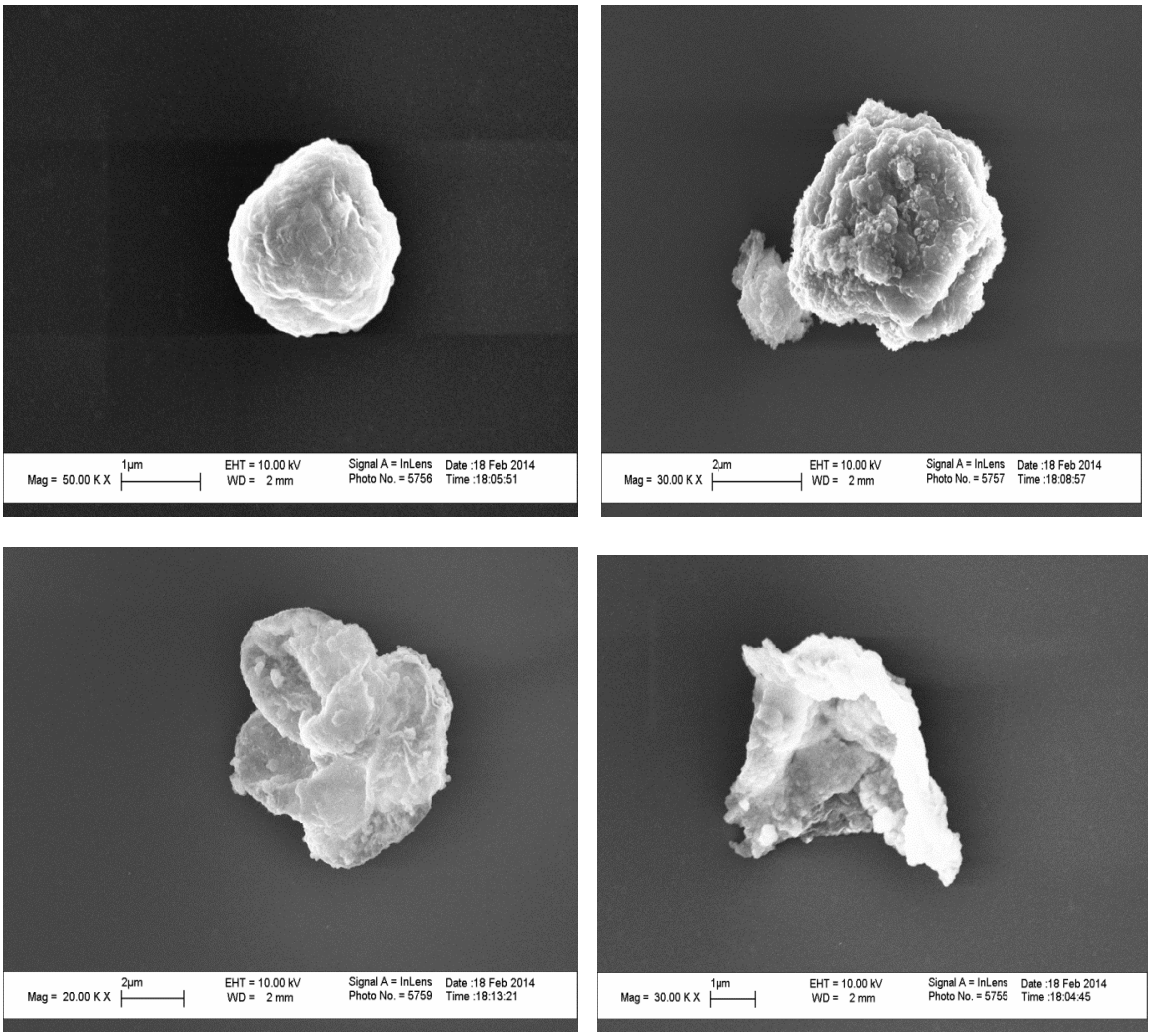

Figure 3.4 SEM images of combustion products of 1-11 µm powder collected from air-acetylene flame.

The diameters of most condensed product particles collected from the acetylene flame are in a range of 2 to 4 µm. The particle sizes of the product from the coarser powder appear to be respectively greater than those for fine starting magnesium powder. For both coarse and fine powders, most of the product particles are not spherical. There fewer spherical particles in the products produced by the finer Mg powder.

In some images of the product particles (see right hand side of Figure 3.3), a cloud of finer particles around the coarser product particle is observed. This cloud could be indicative of

the condensation from the vapor phase flame. Such clouds are almost undetectable in the products formed by the finer Mg powder.

3.3 Burn Times as a Function of Particle Size

As noted above, superficial readings indicative of very fine particles were obtained in size distribution measurements. When the size distributions accounting for these readings were taken to process the burn time experiments, there was a large number of very fine particles, which biased the implied burn times considerably. The effect of correction of the particle size distribution on the burn times for the 1 – 11 μm powder is illustrated in Figure 3.5. Only corrected size distributions were used in the subsequently presented results.

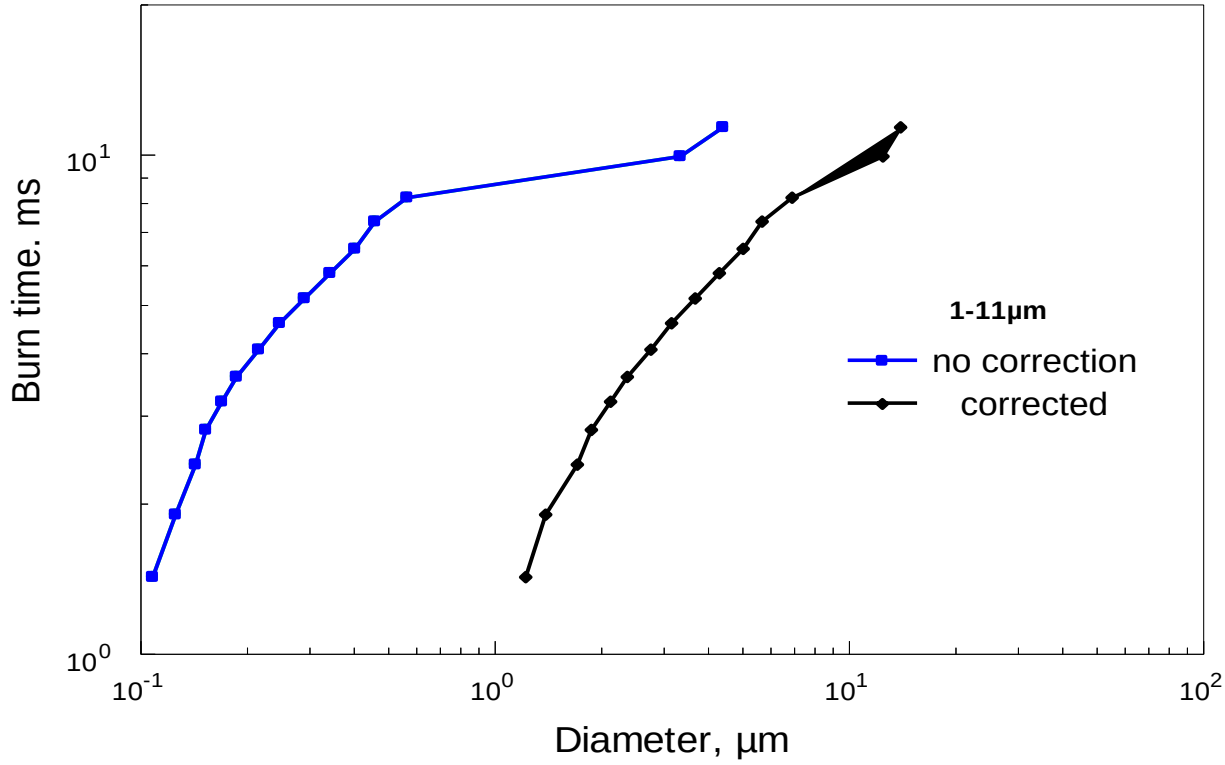

Figure 3.5 Particle burn time versus particle size with and without correcting size.

Burn times for different as-received powders measured for different turbulence levels are shown in Figure 3.6. The set of plots shown on top accounts for all particle emission pulses, including outliers, which could be removed, as illustrated in Figure 2.11 and Figure 2.12. The same data processed with the outlier points removed are shown in the bottom set of plots in Figure 3.6. It is apparent that the outlier points result in an unrealistically strong effect of particle size on burn time for the finest particles – for each powder batch. Once the outlier points are removed, the main trend for the effect of particle size on burn time remains nearly unchanged; however, the sharp effect for fine particles disappears.

For both coarse and fine powders, the higher turbulence levels result in the shorter burn times. The effect of turbulence on burn time appears to be stronger for finer particles. For -325 Mesh powder, the burn times for largest particles are not apparently affected by the flow conditions.

The most unexpected result is that the burn times are not the same for the same size particles from different powder batches. Particles from the 1-11 μm powder are burning longer than the same size particles from the -325 Mesh powder under identical flow conditions.

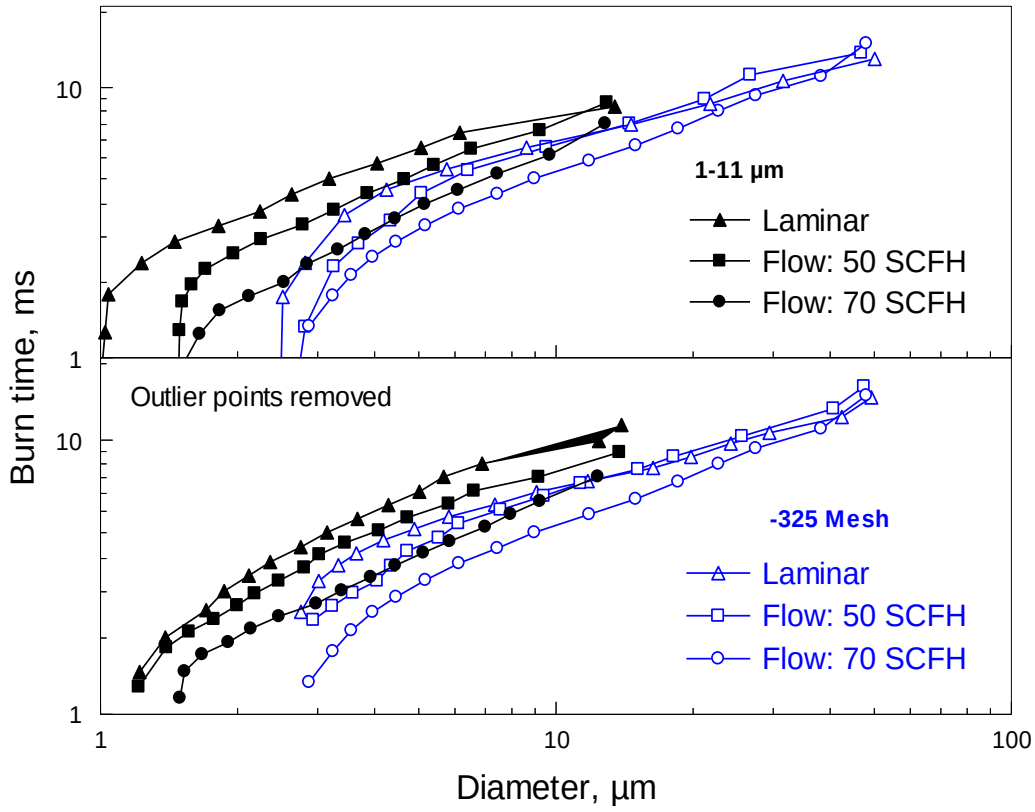

Figure 3.6 Burn times versus particle diameters for fine and coarse powders in different turbulent levels.

The effect of powder aging on the particle burn times is shown in Figure 3.7, where data for the laminar flame experiments are presented. The effect of aging appears to be negligible for the coarsest and finest particles in the batch, however, aged particles with intermediate sizes burn slightly longer than the same size "as received" particles. It may also be noted that the effect of particle size on the burn time for the aged particles is slightly weaker than for the "as received" powder.

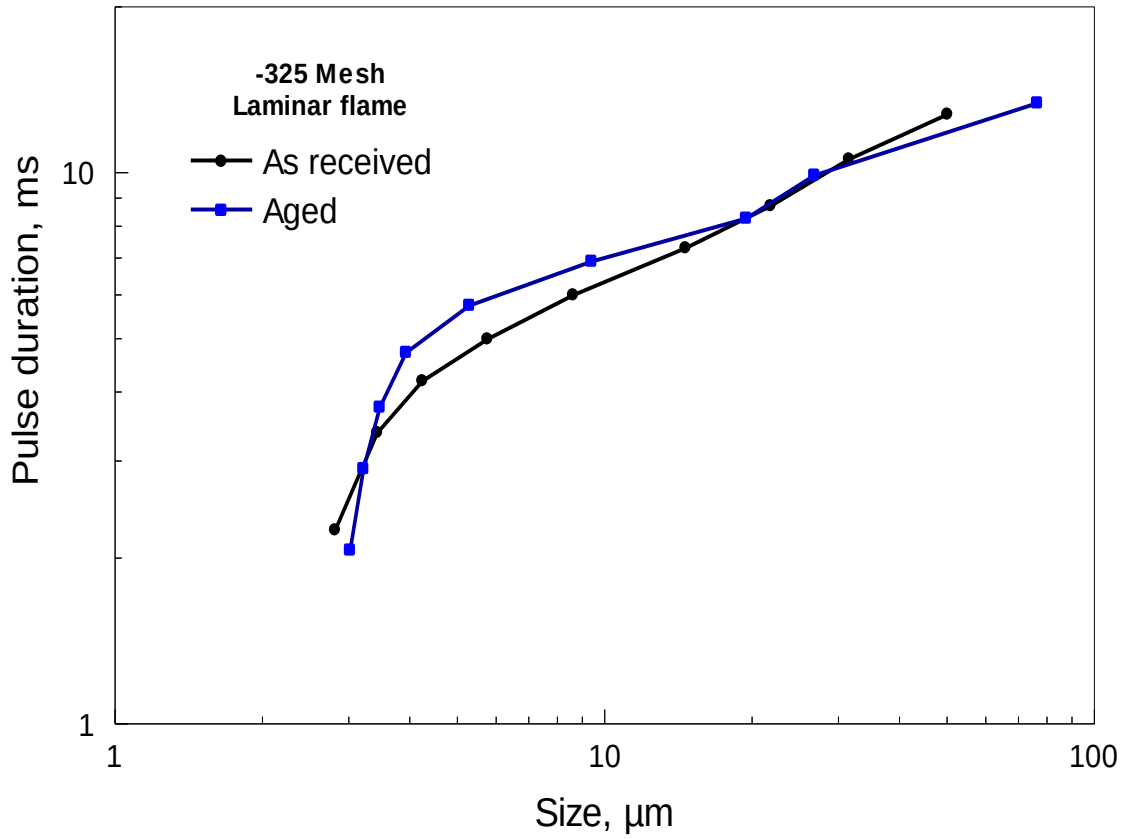

Figure 3.7 Burn times versus particle diameters for aged and fresh powders (-325 Mesh).

3.4 Particle Temperatures

Particle combustion temperatures were obtained for a representative subset of the recorded emission pulses. Results are summarized in Table 3.1. For the finer, 1 – 11 µm powder, the temperatures were varied in a relatively narrow range of 1900 – 2300 K for all flow conditions. The temperatures increased slightly with an increased level of turbulence. For the coarser powder, the temperatures were markedly higher for the laminar flow, reaching as high a 2900 K, while for the turbulent flames the temperatures were lower, from 2050 to 2300 K.

Table 3.1 Combustion Temperature for Magnesium Powders Burning in an Acetylene-air Flame at Different Turbulence Levels.

	Magnesium -325 Mesh	Magnesium 1-11 μm
Particle combustion temperature in laminar flame	2500-2900 K	1900-2100 K
Particle combustion temperature in 50 SCFH turbulence flame	2050-2300 K	1900-2050 K
Particle combustion temperature in 70SCFH turbulence flame	2050-2300 K	2050-2300 K

A correlation between the measured temperatures and individual particle burn times is shown for a selected subset of emission pulses in Figure 3.9. For the -325 Mesh powder, both burn times and temperatures appear to be noticeably longer for the laminar flame experiment. A trend between longer burn times and temperatures is also observed considering all data points shown. No such trend is apparent for the 1 – 11 μm powder.

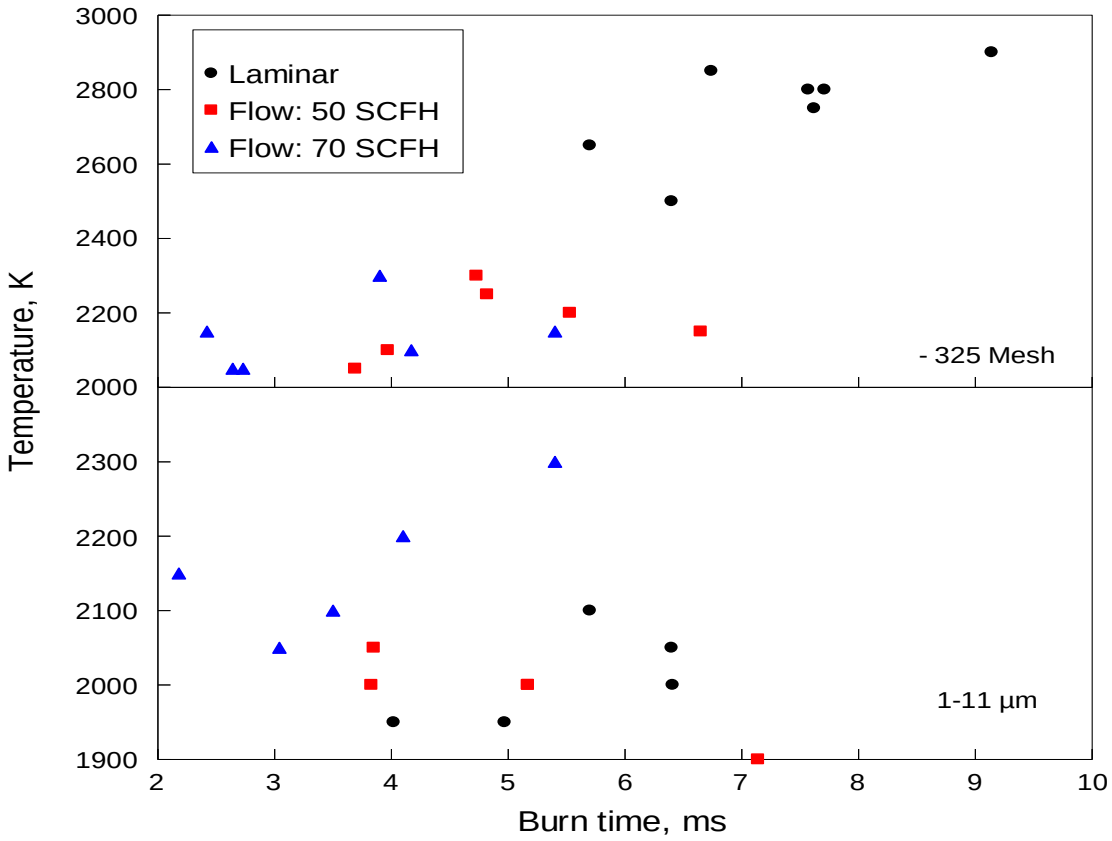

Figure 3.9 Temperature versus burn time for particle pulses recorded for different powders and different turbulence levels.

CHPATER 4

DISCUSSION

4.1 Effective Oxide Thickness

Results of thermo-gravimetric measurements for oxidation of Mg powders indicate that the final weight gain is slightly different for different powders, indicating a difference in the amount of oxide present in the powders initially. In Table 3.1, these differences are interpreted in terms of different effective thickness of the MgO layer coating the powder. As shown in the SEM images in Figure. 2.4 at least part of the MgO initially present in the as-received powders exists as small particles or particle agglomerates attached to the particle metal surfaces. The metal surface, which must be covered by a thin MgO layer that is not directly resolved by the SEM images, appears to be similarly smooth for both as-received powders. The surface morphology changes for the powders subjected to aging, where patches that appear to be more oxidized appear. Based on the above observations, it is likely that the difference in the effective oxide thickness between different as-received powders described in Table 3.1 represents the difference in the amount of the fine attached MgO particles or agglomerates rather than the difference in the continuous MgO layer covering metal surface.

4.2. Effect of the Apparent Initial Oxide Thickness on the Burn Times

Results shown in Figure 3.3 suggest that different burn times were observed for the same size particles from different magnesium powder batches. This result was unexpected because particles with the same initial size should have the same burn times.

Results shown in Figure 3.4 and Table 3.1 show that the apparent thickness of the initial MgO layer for the two powders was not the same. The particles that had a greater initial effective oxide thickness or, as discussed above, had a greater amount of fine MgO particles adhered to their surfaces, were observed to burn longer. A slight increase in the burn times is also observed when aged powder is compared to its as received counterpart (Figure 3.4).

The effect of the slight initial difference in the apparent MgO film thickness on the particle burn time is surprising. Indeed, Mg particles are expected to burn in the vapor phase, which is generally supported by their measured flame temperatures that always well exceed the Mg boiling point (1364 K or 1091 °C). The initial MgO layer is not expected to retain any protective interface properties once the combustion begins. Thus, correlation between its initial effective thickness and the burn time is unlikely.

A possible explanation of the effect of the effective oxide thickness on the burn times may be offered considering that, unlike other metal oxides, MgO remains solid during combustion, and that, as discussed above, the difference in the effective thickness is likely to represent the difference in the amount of fine MgO particles adhering to the metal surface. Because MgO does not melt, it is expected that early on, when Mg begins boiling, the initial MgO layer disintegrates and, together with the MgO particles adhered to the metal surface, forms solid islands or inclusions in the burning molten Mg particle. The amount and sizes of the MgO particles present initially affect the size and morphology of the formed inclusions.

Magnesium evaporation is blocked by the MgO islands on its surface; thus particles with greater portion of their surface blocked by MgO inclusions are likely to burn slower when the vapor-phase combustion is being developed (e.g., boiling point of Mg is achieved). Furthermore, the MgO inclusions formed initially are expected to serve as preferred condensation areas for the MgO formed in the vapor-phase combustion. Indeed, the flow of MgO back to the burning particle surface is opposed by the flow of evaporating magnesium; however, no such flow exists from the MgO islands. Thus, the initially formed islands are likely to grow during particle combustion, and thus their initial sizes and morphology may define how fast they are growing and how much more surface of the burning particle is blocked during its combustion.

A greater amount of MgO initially present in the 1 – 11 μm powder, inferred from its greater effective MgO thickness, is thus likely responsible for the lower evaporation rates and observed longer burn times for the particles of this powder compared to their counterparts from the coarser and less oxidized -325 Mesh powder.

This reasoning is supported by the non-spherical shapes of the quenched combustion product particles. The particle shapes are distinctly non-spherical for the finer powder, which initially contained greater amount of adhered ultrafine MgO particles. This suggests a rapid growth of the initial solid MgO islands so that such islands begin dominating the overall shapes of the burning particles. Conversely, more rounded particle shapes are observed for the coarser particles from the as-received -325 Mesh powder, suggesting that the particles evaporate more uniformly and that smaller fraction of their surface is blocked by MgO islands. It is also interesting that the clouds of ultrafine condensed particles are detected around coarser product particles for the -325 Mesh powder, for which the burn rates are greater. No such clouds were observed around the particles from the 1 – 11 μm powder, which could be interpreted that bulk

of the condensate returned to the particle surface and condensed there, increasing the dimensions of the MgO islands and resulting in a greater distortion of the particle shapes from spherical, and in a more suppressed evaporation rates.

4.3 Comparisons with the Burn Times for Mg Reported in the Literature

The author found no reports identified magnesium particle burn times in acetylene-air combustion products. There some publications identified magnesium particle burn times in water and most of such reports dealt with powders that were coarser compared to those used here. Results of the present experiments are shown in Figure.4.3.1, together with several data sets found in the literature [26, 28, 31, 46, 47].

A recent study [24] used very large 1.5 – 5 mm particles ignited with a hot wire. Water vapor balanced with argon was supplied into the combustor chamber. Partial water pressure was 0.05 MPa. A high speed camera was used to observe the flame structure and combustion process. The results produce a trend line described by $t \sim d^2$ relationship (or d^2 law), where t is the burn time and d is particle diameter.

Results, from earlier experiments [47] also fit well with the $t \sim d^2$ trend line reported in Reference [24]. Prachukho [47], produced water vapor using a flat flame H_2 / O_2 burner with an addition of nitrogen to vary the water concentration. The flame was placed in an enclosed environment. Water temperature was assessed to be about 1373 K. Magnesium particles were fed into the flame. The particle sizes of the powder used varied between 1 and 250 μm; however, the powder was size classified into six fractions: –40, 37–64, 66–116, 86–133, 102–152, and 144–205 μm. Burn times were recorded on a continuously moving film and measured using a rotation disk as a shutter.

Another relevant experiment has been reported in Reference [29]. Free-falling individual magnesium particles were produced and ignited using a pulsed micro-arc and burned in air. Monodisperse metal droplets were studied with predetermined diameter in the 250 to 400 μm range. Particle radiation was monitored using a fiber optic trifurcated bundle fed to three HC120-01 Hamamatsu photosensor modules, equipped with an interference filter. Combustion times in air were in the range of 70 – 160 ms for the magnesium particles with diameters in the range of 250 – 400 μm and the results are well fit with the d^2 law.

Evaluation of measurements of the burn times of magnesium particles (50 to 120 μm), burn in oxygen, air, $2O_2 + 8Air$, and $2O_2 + 8He$ have been done in Ref. [48]. A Vycor tube contained in a vertical Nichrome wire furnace (64 cm long) was filled at atmospheric pressure with oxygen, air, premixed $2O_2 + 8Air$ or $2O_2 + 8He$ respectively. Classified magnesium particles ranging in diameter from 20 to 120 microns were dropped into the furnace by tapping from a fine screen of proper size to prevent passage of agglomerates. Furnace temperature was maintained near 1200 K. The results, presented Figure 4.1 show that the same magnesium powder particles burn in gases with different oxygen/diluent compositions following the same d^2 law.

The combustion mechanism of laser-ignited magnesium particles in the 100 μm size range was studied by cinematography of burning particles and by scanning electron microscopy of quenched samples in Refenrece [31]. Burning was investigated in room temperature, atmospheric pressure, oxygen argon atmospheres, with oxygen mass fractions ranging from 0.03 to unity. Briefly, a single particle of 100 mesh size is suspended at the tip of a glass fiber by natural adhesive forces. The powders used have particles of highly irregular shapes, with the majority in the form of chips; relatively regular particles with equivalent diameters between 50

and 200 μm were selected. Ignition is achieved by using a neodymium-doped glass laser. The irregular burning histories and the nonspherical shapes of the burning particles prevent from testing a d-square law by plotting particle diameter as a function of time. The most quantitative type of data that could be obtained readily from results was the total time to extinction as a function of the initial particle diameter. The plot showing the extinction time versus initial particle diameter followed a d^2 law.

This experiment described here result in longer burn times and a weaker effect of powder size on the burn time compared to those expected for fine Mg particles based on the literature data. Using a conventional $t \square d^n$ law, present experiments for magnesium powder 1-11 μm and magnesium Mesh-325 powder are described reasonably well when $n \approx 0.75$ and 0.80, respectively. A recent study [35] was performed with fine 1 - 11μm magnesium powders and using the same experimental setup. Particles burned in water vapor. Particles were injected into products of a hydrogen/oxygen flame and particle emission signatures were recorded with interference filters. The resulting burn times were described reasonable well when $n \approx 0.68$ which is close to the present experiments using the same fine Mg powder.

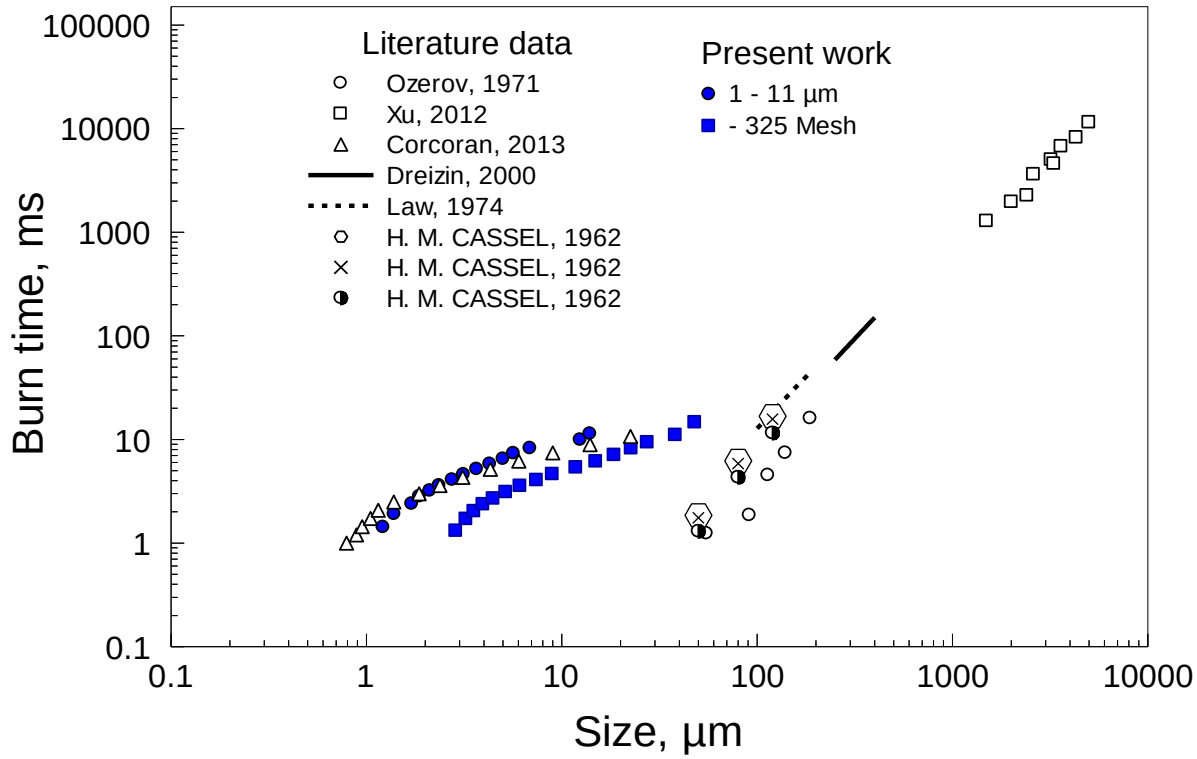

Figure 4.1 Burn times versus particle sizes.

Present results show a markedly reduced effect of particle size on the burn time compared to most of the earlier experimental studies, focused on substantially coarser particles. At the same time, a reduced effect of particle size on the burn times of metal particles was observed recently for a broad range of powders, including aluminum [36-38, 49], zirconium, titanium [50], and some of the mechanically alloyed powders [51]. Thus, it is likely that the reduced effect of particle size on burn times for fine metal particles is associated with generic modifications in the heat and mass transfer processes for such particle sizes, rather than with specific kinetic combustion limitations for specific fuels.

It was shown recently that for the transition regime of transport phenomena occurring for particles with dimensions comparable to the mean free path of gas molecules, the rates of heat and mass transfer from the burning particles are impeded substantially compared to those

occurring in the continuous transport regime [52]. Previous theoretical models did not account for the complex phenomena occurring in magnesium combustion and involving combined evaporating and condensing mass flows from and to the particle surface. For example, an effect of condensed MgO blocking part of the metal surface from evaporation, which was observed to be stronger for finer particles, could be responsible for the increasingly long burn time for such particles. Further work aimed at development of detailed theoretical models involving complex transport phenomena occurring in combustion of Mg is needed for more detailed interpretation of the present results.

4.4 Effect of Turbulence on the Observed Particle Burn Times

In qualitative agreement with the previous experiments with aluminum powders [39], greater levels of turbulence resulted in shorter burn times for all powders, as shown in Figure 3.7. However, the effect of turbulence was clearly diminished for the coarser fraction of the -325 Mesh powder. This may be interpreted by suggesting that the coarsest particles were burning long enough to exit from the combustion product of air/acetylene flame and thus be oxidized primarily by oxygen from the surrounding air. At the same time, they were burning along the centerline of the experimental setup, directly above the air/acetylene flame, so that the surrounding gas temperature remained high, unlike the temperature of air mixing rapidly with the combustion products of the air/acetylene flame in experiments with the induced flow turbulence.

It is interesting that the effect of turbulent mixing appears to be weaker for the burn rates of magnesium addressed here compared to that observed earlier for aluminum [39]. This observation may need to be considered together with the temperature measurements, indicating

lower flame temperatures for Mg particles in the flows with higher turbulence levels. Thus, the effect of an enhanced mixing in the more turbulent flows might have been offset by the reduced reaction temperature. Such differences are expected to be interpreted in the future work aimed at development of detailed combustion dynamics models for different metals.

4.5 Combustion Temperatures

Although the present data on combustion temperatures are preliminary in nature, some interesting features of the magnesium particle combustion are revealed. For all cases, the measured temperatures exceed substantially the boiling point of Mg; thus, the effect of vapor-phase combustion must be strong for all present experiments. However, except for the coarser particles burning in the laminar environment, the measured temperatures are substantially lower than the adiabatic flame temperature for magnesium. This suggests that the vapor phase flame may not be the only or even the dominant mode of combustion for fine magnesium particles considered here. Released Mg vapors may react with oxidizers while in immediate vicinity of the particle surface and condense directly on the surface, resulting in a quasi-heterogeneous reaction. Reaction may also occur while the vapors diffuse through porous MgO inclusions, so that the condensed reaction products form directly in such pores. In both cases, no classic standoff vapor phase flame is formed.

It is unclear whether the measured temperatures represent the temperatures of the burning particles or those of the condensed combustion products. In the former case, it is possible that the MgO islands and inclusions are heated substantially above the Mg boiling point. This scenario is consistent with the observed decrease in the measured temperature with an increased level of turbulence, resulting in a more effective cooling of the hot MgO

inclusions. Furthermore, this is consistent with the observed weak effect of the turbulence on the burn rate. While mixing in the gas phase is improved with the increased turbulence, cooling off the MgO inclusions reduces the thermal driving force for evaporation of the molten Mg, so that the increase in the burn rate is relatively weak.

CHPATER 5

CONCLUSION

An experimental technique for measuring metal particle burn times in the combustion products of air-acetylene flame at different flow turbulence levels is adapted for studying combustion of micron-sized particles of Mg. For particles in the size range of 1 – 50 μm, the effect of particle sizes, d, on the burn times, τ, is reasonably well described by a $\tau \sim d^{0.8}$ trend. This effect is much weaker than the trend of $\tau \sim d^{2}$ reported earlier for coarser Mg particles, but is consistent with recent results for burn times of fine particles of other metals. Combustion rates were affected by the flow turbulence, with increased burn rates observed for flow conditions with greater turbulence levels. The temperatures of the burning particles decreased with increase in the flow turbulence. Combustion temperatures measured in the turbulent flows exceeded the Mg boiling point, but were substantially lower than the adiabatic flame temperature. Combustion products collected from the flame comprised mostly non-spherical fine particles.

Burn times for the particles of the same sizes from different powder batches used in the present experiments were not the same. Particles of the 1 – 11 μm powder burned longer than the same size particles of the -325 Mesh powder, although both powders were obtained from the same supplier. It was observed that the 1 – 11 μm powder contained a greater initial MgO fraction. The additional MgO was present in the shape of fine particles adhered to the metal surface. It is hypothesized that the presence of greater amount of fine MgO particles in the starting powder affects the morphology and thus evaporation rates of the burning Mg particles.

It is further suggested that initial differences in the particle morphology affect the rate of condensation of the combustion products on the burning particle, which, in turn, results in further modification of the particle shape. It is proposed that differences in the particle shapes caused by MgO islands and inclusions and respectively different fractions of the metal surface blocked by the oxide, and thus unable to generate the flow of Mg vapor, result in the different measured burn rates for different Mg powder batches.

REFERENCES

[1] H. Habu, Keikinzoku, 58 (2008) 162-166.

[2] L.T. De Luca, L. Galfetti, D. Signoriello, S. Levi, S. Cianfanelli, V.A. Babuk, G.F. Klyakin, V.P. Sinditskii, A.B. Vorozhtsov, Valencia, 2006, pp. 6570-6582.

[3] L.T. De Luca, L. Galfetti, F. Severini, M. Galeotta, R. De Amicis, V.A. Babuk, B.N. Kondrikov, A.B. Vorozhtsov, in: A. Wilson (Ed.), Sardinia, 2004, pp. 143-148.

[4] E.W. Price, Combustion of Metallized Propellants, AIAA, New York, 1984.

[5] Z. Zarei, D.L. Frost, Shock Waves, 21 (2011) 425-438.

[6] M.F. Gogulya, M.N. Makhov, M.A. Brazhnikov, A.Y. Dolgoborodov, V.I. Arkhipov, A.N. Zhigach, I.O. Leipunskii, M.L. Kuskov, Combustion, Explosion and Shock Waves, 44 (2008) 198-212.

[7] D.L. Frost, M. Cairns, S. Goroshin, F. Zhang, Waikoloa, HI, 2007, pp. 781-784.

[8] H.D. Jones, F.J. Zerilli, Publ by Materials Research Society, 1993, pp. 311-315.

[9] S. Nacu, Revista de Chimie, 62 (2011) 113-115.

[10] A.G. Rajendran, C.B. Kartha, V.V. Babu, Defence Science Journal, 50 (2000) 199-206.

[11] K.J. Smit, R.J. Hancox, D.J. Hatt, S.P. Murphy, L.V. De Yong, Applied Spectroscopy, 51 (1997) 1400-1404.

[12] A.A. Zenin, G.P. Kuznetsov, V.I. Kolesnikov, Khim. Fiz., 30 (2011) 28-41.

[13] T.A. Roberts, R.L. Burton, H. Krier, Combust. Flame, 92 (1993) 125-143.

[14] A.L. Breiter, E.I. Popov, V.L. Velikanova, Fiz. Aerodispersnykh Sist., 23 (1983) 43-48.

[15] S. Yuasa, T. Takeno, Symp. (Int.) Combust., [Proc.], 19th (1982) 741-748.

[16] E.I. Popov, L.Y. Kashporov, V.M. Mal'tsev, A.L. Breiter, Fiz. Goreniya Vzryva, 9 (1973) 240-246.

[17] A.L. Breiter, L.Y. Kashporov, V.M. Mal'tsev, P.F. Pokhil, E.I. Popov, V.I. Pepekin, A.G. Stasenko, Fiz. Goreniya Vzryva, 7 (1971) 222-227.

[18] V.G. Poyarkov, Izv. Vyssh. Ucheb. Zaved., Tsvet. Met., 10 (1967) 149-153.

[19] S.M. Umbrajkar, M. Schoenitz, S.R. Jones, E.L. Dreizin, Journal of Alloys and Compounds, 402 (2005) 70-77.

[20] Y. Aly, M. Schoenitz, E.L. Dreizin, Combustion and Flame, 160 (2013) 835-842.

[21] P.J. Miller, Materials Research Society, Boston, MA, USA, 1996, pp. 413-420.

[22] R.A. Yetter, G.A. Risha, S.F. Son, Montreal, QC, 2009, pp. 1819-1838.

[23] E.L. Dreizin, Combustion and Flame, 116 (1998) 323-333.

[24] X. Huang, Z.-x. Xia, L.-y. Huang, J.-x. Hu, Hanneng Cailiao, 21 (2013) 379-386.

[25] A.E. Valov, Y.A. Kustov, V.I. Shevtsov, Fiz. Goreniya Vzryva, 30 (1994) 29-35.

[26] E.L. Dreizin, C.H. Berman, E.P. Vicenzi, Combustion and Flame, 122 (2000) 30-42.

[27] V.I. Shevtsov, V.P. Fursov, L.N. Stesik, Fiz. Goreniya Vzryva, 12 (1976) 859-856.

[28] G.K. Ezhovskii, A.S. Mochalova, E.S. Ozerov, A.A. Yurinov, "Nauka", 1972, pp. 234-240.

[29] E.L. Dreizin, V.K. Hoffmann, Combustion and Flame, 118 (1999) 262-280.

[30] A.V. Florko, V.V. Golovko, N.A. Okhrimenko, V.G. Shevchuk, Combustion, Explosion, and Shock Waves, 27 (1991) 32-37.

[31] C.K. Law, F.A. Williams, Combustion and Flame, 22 (1974) 383-405.

[32] N.I. Poletaev, Combustion, Explosion and Shock Waves, 48 (2012) 151-162.

[33] K.L. Cashdollar, I.A. Zlochower, J. Loss Prev. Process Ind., 20 (2007) 337-348.

[34] J.E. Tanner, Jr., Nav. Ammunition Depot, 1974, pp. 24 pp.

[35] A.L. Corcoran, S. Mercati, H. Nie, M. Milani, L. Montorsi, E.L. Dreizin, Combustion and Flame, submitted (2013).

[36] C. Badiola, E.L. Dreizin, Combustion Science and Technology, 184 (2012) 1993-2007.

[37] C. Badiola, R.J. Gill, E.L. Dreizin, Combustion and Flame, 158 (2011) 2064-2070.

[38] R.J. Gill, C. Badiola, E.L. Dreizin, Combustion and Flame, 157 (2010) 2015-2023.

[39] A.L. Corcoran, V.K. Hoffmann, E.L. Dreizin, Combustion and Flame, 160 (2013) 718-724.

[40] D. Bradley, Z. Chen, J.R. Swithenbank, Symposium (International) on Combustion, 22 (1989) 1767-1775.

[41] R.K. Kumar, E.M. Bowles, K.J. Mintz, Combustion and Flame, 89 (1992) 320-332.

[42] W. Arnold, E. Rottenkolber, Int. Annu. Conf. ICT, 40th (2009) 37/31-37/10.

[43] A. Cezairliyan, S. Krishnan, J.L. McClure, Int. J. Thermophys., 17 (1996) 1455-1473.

[44] R.M. Pon, J.P. Hessler, Appl. Opt., 23 (1984) 975-976.

[45] J.C. de Vos, Physica (The Hague), 20 (1954) 690-714.

[46] I. Liebman, J. Corry, H.E. Perlee, Combust. Sci. Technol., 5 (1972) 21-30.

[47] V.P. Prachukho, E.S. Ozerov, A.A. Yurinov, Combustion, Explosion and Shock Waves, 7 (1971) 195-198.

[48] H.M. Cassel, I. Liebman, Combustion and Flame, 6 (1962) 153-156.

[49] P. Lynch, H. Krier, N. Glumac, Proceedings of the Combustion Institute, 32 (2009) 1887-1893.

[50] C. Badiola, E.L. Dreizin, Proceedings of the Combustion Institute, 34 (2013) 2237-2243.

[51] E.L. Dreizin, C. Badiola, S. Zhang, Y. Aly, International Journal of Energetic Materials and Chemical Propulsion, 10 (2011) 22.

[52] A. Ermoline, D. Yildiz, E.L. Dreizin, Combustion and Flame, (2013).